Master's thesis

2019

Karoline Bråten

NTNU
Norwegian University of
Science and Technology
Faculty of Natural Sciences
Department of Physics

Karoline Bråten

Nanoparticle-stabilized microbubbles and focused ultrasound for targeted drug delivery to tumours

Characterization in the chicken chorioallantoic membrane model

June 2019

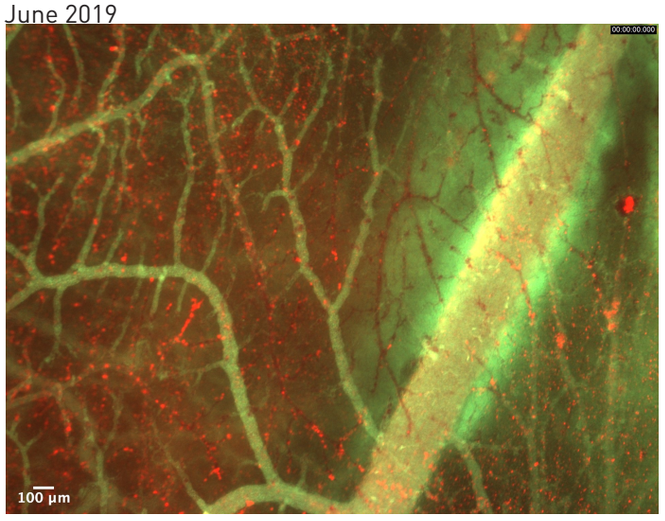

NTNU
Norwegian University of
Science and Technology

NTNU
Norwegian University of
Science and Technology

NTNU

Norwegian University of
Science and Technology

Nanoparticle-stabilized microbubbles and focused ultrasound for targeted drug delivery to tumours

Characterization in the chicken chorioallantoic membrane model

Karoline Bråten

Nanotechnology
Submission date: June 2019
Supervisor: Catharina de Lange Davies
Co-supervisor: Sofie Snipstad

Norwegian University of Science and Technology
Department of Physics

Abstract

The aim of this work was to investigate the behaviour of nanoparticle-stabilized microbubbles (NPMBs) when subjected to pulsed ultrasound (US) in both normal and tumourous vasculatures. The NPMBs were provided by the Department of Biotechnology and Nanomedicine at SINTEF in Trondheim, and had an average diameter of 2.2 μm and an average concentration of $6.0{\cdot}10^8$ MBs/mL. The nanoparticles (NPs) consisted of poly (2-ethylbutyl cyanoacrylate) (PEBCA) and were 100-200 nm in diameter. The chicken chorioallantoic membrane (CAM) model was grown *ex ovo* and utilized to study extravasation, bursts and accumulation of NPs in the vasculature of the CAM. Effects of US on the properties of the vasculature were also studied.

To prepare the *ex ovo* cultures, fertilized chicken eggs were incubated in weighing boats and after six days inoculation of OHS cells (an osteosarcoma cell line) was performed. On day 13 after incubation the delivery of NPs was studied using real-time epifluorescent imaging of the vasculature. During the experiment process a vessel of the CAM was catheterized, 2 MDa fluorescein isocyanate (FITC) dextrans and NPMBs were serially injected into it, and another area of the vasculature was exposed to an US treatment with a mechanical index (MI) of 0.4. The purpose of the dextrans was to visualize the blood vessels during imaging. Images from the experiments were analyzed using the Fiji version of ImageJ.

16 distinct phenomena were observed and 12 of them studied in greater detail. Events of both slow extravasation and burst extravasation was found for one of the CAMs. Various patterns of NP accumulation were observed, in addition to a vascular site with hindered perfusion which displayed extensive NP accumulation in the whole FOV. Vasoconstriction and changes in the direction of blood perfusion were common features in the vasculatures. One CAM portrayed leaky blood vessels and dark spots prior to US treatment.

Combining NPMBs and US in this platform for targeted drug delivery to tumours is a promising approach, as it seemed to increase desirable effects in vasculatures.

Sammendrag

Formålet med dette arbeidet var å undersøke oppførselen til nanopartikkel-stabiliserte mikrobobler (NPMBer) når de ble utsatt for pulsert ultralyd (UL) i både normale og kreftutsatte blodkar. Alle NPMB-batcher ble laget av samarbeidspartnere ved SINTEF sin avdeling for bioteknologi og nanomedisin i Trondheim. Disse NPMBene hadde en gjennomsnittlig diameter på 2.2 μm samt en gjennomsnittlig konsentrasjon på $6.0 \cdot 10^8$ MBer/mL. Nanopartiklene (NP) bestod av poly (2-etyl-butyl cyanoacrylat) (PEBCA) og var 100-200 nm i diameter. Korioallantoiske membraner (CAM) fra kyllinger ble utviklet *ex ovo* og benyttet til å studere ekstravasering og NP-akkumulering i CAMenes blodårer. Effektene som UL hadde på egenskapene til blodkarene ble også studert. For å forberede CAM-kulturene ble befruktede kyllingegg inkubert i veieskip og etter seks dager ble de inokulert med OHS-celler (en cellelinje fra et osteosarkom). På dag 13 etter inkubering ble leveringen av NPer studert ved å bruke sanntids epi-fluorescerende avbildning av blodkarene. Kateterisering av en CAM-blodåre ble utført og 2 MDa fluorescein isocyanat (FITC) dekstraner og NPMBer ble serie-injisert i den, og et annet område av blodkarene ble utsatt for en UL-behandling med en mekanisk indeks (MI) på 0.4. Formålet med dekstranene var å visualisere blodkarene under forsøket. Bildeserier fra eksperimentene ble analysert i Fiji-versjonen av ImageJ. 16 distinkte fenomener ble observert og 12 av dem ble studert nærmere. Tilfeller av både sakte og rask ekstravasering ble observert for en CAM. Forskjellige mønstre av NP-akkumulering ble observert i de øvrige resultatene, i tillegg til at et vaskulært område med begrenset perfusjon viste omfattende akkumulering av NPer i hele det avbildede området. Innsnevring av blodkar og endringer i retning av blodstrøm var vanlige observasjoner i blodårene. En CAM viste spesielt lekke blodkar og mørke flekker før UL-behandling. Kombinasjonen av NPMBer og UL for levering av medisiner til kreftsvulster antas å være en lovende tilnærming, da det ser ut til å utløse de ønskede effektene.

Preface

This thesis was submitted as part of a Master of Science in Nanotechnology, with specialization Biotechnology, at the Norwegian University of Science and Technology (NTNU). The work was carried out at the Department of Physics during the spring of 2019. It was part of a collaboration between NTNU and SINTEF, and in continuation of my specialization project conducted in the autumn of 2018. Parts of this thesis is therefore similar to the report written for previous work.

I would like to thank my supervisior Catharina de Lange Davies for excellent guidance through the work of this master's thesis. I would also like to thank Sofie Snipstad for help with lab work and report writing, Kristin Grendstad for providing me with OHS cells, Astrid Bjørkøy for guidance on confocal imaging, and Ellen Helgeland Nymark for help with CAM culturing, experiments and image analysis. My gratitude also goes towards the rest of the biophysics group at NTNU for great discussions and invaluable input on how to interpret all the data obtained.

I would also like to thank our cooperation partners at the Department of Biotechnology and Nanomedicine at SINTEF, particularly Anne Hatletveit and Ýrr Mørch, for providing me with nanoparticle-stabilized microbubbles. Thank you so much to Nortura SA for giving us fertilized chicken eggs, without them this work would not have been possible.

List of abbreviations

BBB	Blood-brain barrier
CAM	Chorioallantoic membrane
DC	Duty cycle
DDS	Drug delivery system
DIW	Deionized water
EC	Endothelial cell
ECM	Extracellular matrix
EPR	Enhanced permeability and retention
FITC	Fluorescein isothiocyanate
FUS	Focused ultrasound
MB	Microbubble
MI	Mechanical index
NA	Numerical aperture
NO	Nitric oxide
NP	Nanoparticle
NPMB	Nanoparticle-stabilized microbubble
NTNU	Norwegian University of Science and Technology
PBCA	Poly(butyl cyanoacrylate)
PDI	Polydispersity index
PEBCA	Poly(2-ethyl-butyl cyanoacrylate)
PEG	Polyethylene glycol
PFB	Perfluorobutane
PI	Propidium iodide

PNP	Peak negative pressure
PRF	Pulse repetition frequency
PRP	Pulse repetition period
RBC	Red blood cell
ROI	Region of interest
SEM	Scanning electron microscope
US	Ultrasound
VEGF	Vascular endothelial growth factor

Table of Contents

1 Introduction

According to the International Agency for Research on Cancer 9.6 million people were estimated to have succumbed to cancer in 2018, making it the second leading cause of death worldwide. About 1 out of 6 deaths is due to cancer and the number is expected to rise in the next decades. The annual cost globally was estimated at US$ 1.16 trillion in 2010, where most of it was spent in high-income countries where the treatment services are more accessible. [1; 2] Cancer treatment today is often a long and tedious process with surgery, radiation therapy, and chemotherapy as the most commonly used means of combating the cancer cells. In conventional chemotherapy, the injected drug is distributed equally between all the cells of the body it is able to reach, resulting in overall damage and the estimate that the drug dose reaching the tumour might be as low as 0.001 %. [3] This systemic administration of drugs is one reason for the many unwanted side effects of the treatment. In the battle against these diseases, various research projects are currently ongoing all over the world to develop better drugs and more efficient methods to deliver them.

Nanotechnology is among the fields that has shown promising results and is expected to rise to the occasion as the next-generation platform for drug delivery systems (DDSs) in cancer therapy and other biomedical applications. One of the ways of elevating the fraction of drug affecting the tumour is by using nanoparticles (NPs), microbubbles (MBs) and ultrasound (US). The drug is encapsulated into NPs that form stable shells around MBs. These are administered into the blood stream of the patient, and applying focused ultrasound (FUS) to the target tumour makes the MBs burst and release the drug. Studies have found that this combined mechanism increases drug uptake by up to 250 times compared to traditional chemotherapy. Among the advantages of this drug delivery platform are reduced drug doses, less side effects and relieved remission, while still achieving good results at treating the tumour in question. [4]

The aim of this study is to examine this novel DDS by investigating its effects on both normal and tumourous vasculature treated with US. The primary goal is to study the behaviour of nanoparticle-stabilized microbubbles (NPMBs) insonated in the vasculature of a chicken *in vivo* model. Extravasation of NPs from the blood vessels into the surrounding tumour tissue was of special interest. In terms of drug delivery, the goal is to extravasate the drug as far as possible into the tumour.

The chorioallantoic membrane (CAM) developing on top of the embryos is an advantageous model for this purpose as it provides a suitable tissue composition and easy accessibility of the vessels for experimental manipulation. The final results of this work will give valuable knowledge about how to utilize NPMBs and US in targeted drug delivery to tumours.

2 Theory

2.1 Cancer

Cancer is a collection of diseases characterized by abnormal and uncontrolled cell proliferation, where the mass of overgrown cells is what makes up a tumour. In healthy tissue cell proliferation is a complex and highly regulated process, ensuring that each tissue type maintains its correct size and architecture. Other cells in the vicinity tells a cell when to proliferate and when it is time to prepare for clearance by macrophages or other phagocytes. [5] Cancer cells do no longer respond appropriately to these signals and may become cancerous. Tumourigenesis is often caused by a combination of promoted cell growth and suppressed apoptosis, as a result of oncogenes with a dominant gain of function and tumour suppressor genes with recessive loss of function. These changes in behaviour are driven by mutations in the genome, often acquired over many years which is why cancer is most prevalent in older people. [6]

The deadliest characteristic of cancer is tumour cells spreading from the primary tumour to other parts of the body. This process of forming secondary tumours is called metastasis and is estimated to be responsible for 90 % of cancer deaths. [7]

There are three general types of tumours: benign, premalignant, and malignant. Benign tumours are non-cancerous, non-growing and cannot metastasize. Premalignant ones are not yet cancerous, but can become so. Malignant tumours are cancerous, and have the ability to grow and metastasize. The rapid growth of malignant tumours affects the development of the surrounding vasculature. A continuous access to blood vessels is crucial for the tumour as they supply the cells with oxygen and nutrients, and remove waste products, and the rapid growth calls for more of them. New blood vessels are formed from existing ones through angiogenesis. In normal tissue, angiogenesis is finely tuned by a balance of pro- and anti-angiogenic factors. Tumourous cells corrupt this system by secreting pro-angiogenic factors like vascular endothelial growth factor (VEGF) while simultaneously downregulating vessel growth inhibitors. [8] Tumour blood vessels differ from normal ones in structure, organization and function. The vasculature surrounding normal cells are well organized and consists of evenly distributed blood vessels, ensuring sufficient perfusion of oxygen and nutrients to all cells. The vasculature around the tumour on the other hand, is chaotic and has immature, tortuous and hyperpermeable vessels. [9] This phenomenon is illustrated in Fig. 2.1, with normal vasculature in (a) and tumourous in (b). The images are taken in a scanning electron microscope (SEM).

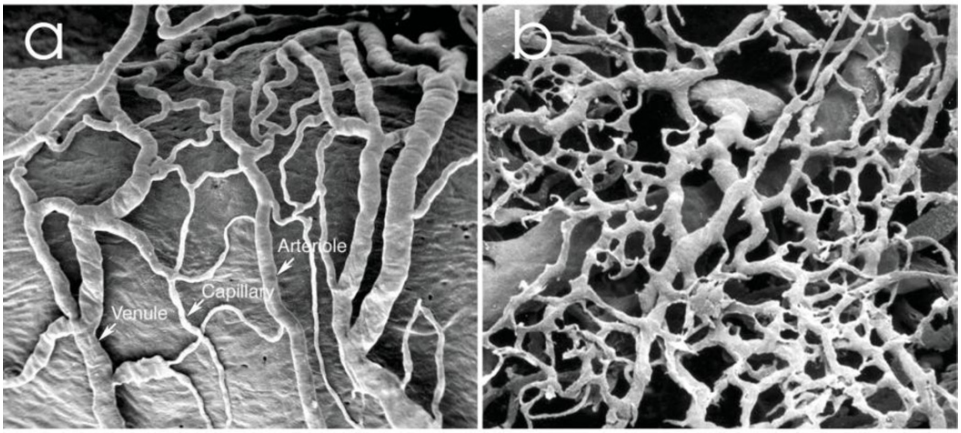

Figure 2.1: SEM images of normal and tumourous blood vessels. (a) SEM image of polymer cast of normal microvasculature (vasa vasorum of rat carotid sinus). (b) SEM image of polymer cast of tumour microvasculature (xenograft of human tumour in nude mouse). The figure is retrieved from Atukorale et al. [10]

2.2 Ultrasound

US was discovered as early as in 1883, but did not find its way into the field of medicine until the 1950s. Today it has a wide range of useful applications such as imaging, dentistry, blood flow analysis, liposuction, tumour and fibroid ablation, kidney stone disruption, and pediatric review. [11] Its non-invasive procedures, good visualization characteristics, and relatively easy management are among the appreciated advantages. On the other hand, US can be harmful to cells and tissues, so careful considerations have to be taken while choosing the appropriate parameters. The term "ultrasound" applies to all acoustic energies with frequencies above 20 kHz, which is considered the limit of human hearing. Typical diagnostic scanners operate with a frequency of 2-18 MHz, where higher frequencies give sonograms with smaller details. A water-based gel is put between the transducer and the patient to couple the US between the two, as direct contact is necessary to transmit the acoustic waves. [12]

2.2.1 Acoustic impedance

The transmission of pressure waves through a medium can act on cells and biomolecules and make the medium compress and expand. Compression is when molecules are moved closer together, while rarefaction is when they are forced further apart. Ultrasonic waves can be reflected, refracted, focused and absorbed, but are absorbed relatively little by water and tissues. [11] In diagnostics, B-mode (brightness mode) images are constructed from US echoes. They are generated by reflection of ultrasonic waves at tissue boundaries, and scattering from small irregularities in the tissues. Distinctive acoustic impedances of different media make some of the waves transmit and some reflect. Acoustic impedance z

of a medium is a measure of the response of the particles of the medium in terms of their velocity, to a wave of a given pressure. Acoustic impedance $z = p/v$, where p is the local pressure and v is the local particle velocity. The acoustic impedance of a medium is also determined by its density (ρ) and stiffness (k), and from this it can be found that $z = \rho c$, where c is the speed of sound. Values of acoustic impedance for air, water and some bodily tissues are shown in Table 2.1. The acoustic impedance of soft tissues and water are quite similar, while for bone it is a little higher. Compared to these, the acoustic impedance of air is very small, and at an interface between air and tissue 99.9 % of the sound waves are reflected due to this large difference. This is the reason for the importance of having a direct contact between the US transducer and the soft tissue to be imaged, with no air in between. [13]

Table 2.1: Values of acoustic impedance for air, water and some tissues. The values are retrieved from Hoskins et al. [13]

Material	**z ($kgm^{-2}s^{-1}$)**
Kidney	$1.64{\cdot}10^6$
Blood	$1.67{\cdot}10^6$
Fat	$1.33{\cdot}10^6$
Bone	$6.47{\cdot}10^6$
Water	$1.48{\cdot}10^6$
Air	430

2.2.2 Generation of ultrasound

The effects US has on living tissues are called bioeffects, and are due to the energy transmitted by the waves. Heating (thermal) and mechanical (non-thermal) effects are the main bioeffects observed. The mechanical index (MI) is a measure of acoustic power, the amount of acoustic energy per time unit, and is defined as

$$MI = \frac{PNP}{\sqrt{F_C}}, \tag{2.1}$$

where PNP is the peak negative pressure (MPa) of the US wave, and F_C its center frequency. It is a measure of the power of the US beam, and arose from the need of an indicator for the possible non-thermal effects of the beam, such as cavitation and streaming. [14] The effects of these on MBs and tissues are discussed in Section 2.4.2. The US beam is generated in a transducer, which converts electrical energy to mechanical energy based on the piezoelectric principle. This property makes the material produce an electrical field if it is mechanically deformed, in an attempt to restore its shape. Conversely, in response to an applied electrical field it will physically deform. [15] US transducers contain multiple piezoelectric crystals that vibrates when an electrical current is applied. These vibrating sound waves create alternating areas of compression and rarefaction when propagating through a medium. [16] The US waves produced in the transducer are shaped as a beam, directing the waves mostly forward. The beam can be focused, meaning that it has a focal point where it is at a minimum width and maximum pressure. [13]

Two basic generation modes are used in medical US: continuous and pulsed. Continuously exciting the transducer with an electrical sine wave at a constant amplitude produces a continuous US signal. In pulsed US, the US is on for a short period of time and off for a longer period of time, and the process is repeated. In imaging, the pause is important in order to detect the echoes. [17]

The pulse duration τ is determined by

$$\tau = NT = \frac{N}{f}, \tag{2.2}$$

where N is the number of cycles or waves per pulse, also called the burst count. The ratio of the pulse duration to the pulse repetition period (PRP) is called the duty cycle (DC). It is the fractional amount of time the pulse is activated, and given by

$$DC = \frac{\tau}{PRP} = \tau PRF, \tag{2.3}$$

where PRF is the pulse repetition frequency, giving the number of pulses emitted per second. [17]

2.3 Microbubbles

MBs are in clinical use as contrast agents in diagnostic US imaging, made possible by their differing acoustic impedance from soft tissues. Additionally, they can be used for therapeutic purposes as they may be utilized together with FUS to increase the permeability of vessels and cell membranes. The field of combining therapeutics and diagnostics is termed theranostics, and is expected to play an increasingly important role in the near future. [18] US contrast agents consist of gas MBs in a solution, and are administered intravenously. Clinically approved MBs typically have a diameter of 1-10 $\mu\mathrm{m}$, and because of their relatively large size they are contained within the vasculature. Tuning of the stability and the corresponding circulation lifetime of the MBs can be done in a number of ways. Firstly, the gas core is composed of a heavy molecular weight inert gas, like SF_6, C_3F_8 or C_4F_10. These have a low solubility in the surrounding medium, giving a prolonged longevity. Secondly, the gas bubbles are coated with a lipid, polymer, sugar, or protein material into a stabilizing layer around them. This reduces the surface tension, and also the corresponding capillary pressure which drives the gas into solution. Furthermore, it provides an advantageous gas diffusion barrier. Drug delivery systems also incorporate drugs onto or in the coating. The coating alters the bubble dynamics, therefore the type of coating must be chosen according to the application and the desired behaviour. Typically, there are two types of coatings: flexible coatings of phospholipids and rigid encapsulations of e.g. polymers. The phospholipid coating has a thickness of a few nanometers, while the rigid coating is typically of a thickness of tens of nanometers. [19] An example of MBs with a flexible coating is the commercial Sonazoid bubbles (GE Healthcare), conventionally used as a contrast agent in US imaging. The microspheres of perfluorobutane (PFB) are stabilized by a monomolecular membrane of hydrogenated egg phosphatidyl serine, embedded in an amorphous sucrose structure. [20] A type of rigid-coated bubbles is the SINTEF NPMBs, presented in the next section.

2.3.1 Nanoparticle-stabilized microbubbles

Nanoparticle-stabilized microbubbles are MBs with stable shells of NPs around them, which enable them to stay in circulation for longer. [19]

Figure 2.2 is a representation of the combination of NPMBs and US as a platform for drug delivery. The NPs are functionalized with polyethylene glycol (PEG) groups, a common approach to avoid clearance by the host's immune system. The typical size range of the diameter of the particles is 100-200 nm. The NPs are versatile, as they can be loaded with a variety of drugs, ligands, dyes and contrast agents. By self-assembly they form stable shells around the MBs, which are typically 1-6 μm in diameter. As the MBs are subjected to US they can release their content at the desired location, e.g. at the site of a tumour. [21]

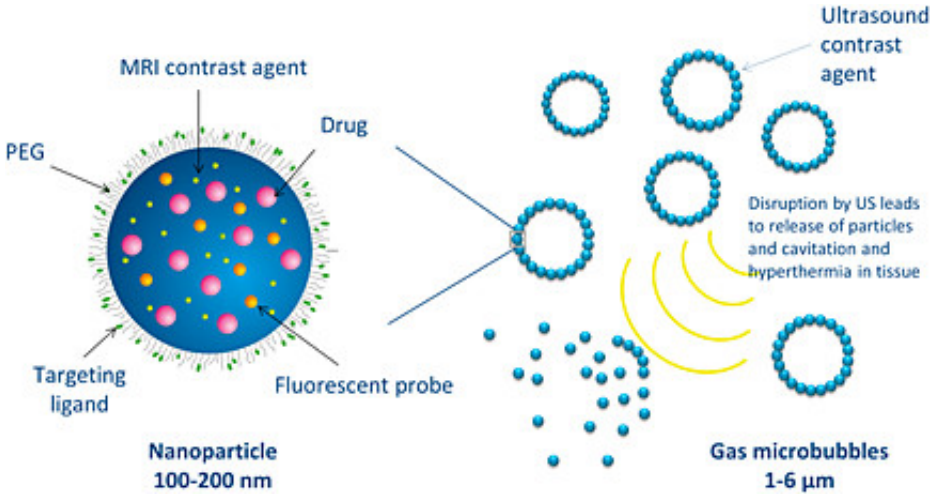

Figure 2.2: NPMBs for drug delivery. The NPs have a diameter of 100-200 nm, are PEGylated, and can be loaded with drugs, dyes and imaging agents. The MBs are 1-6 μm across, and release the NPs at the application of US. The figure is retrieved from MÃ¥rch et al. [21]

Some factors contributing to bubble behaviour are the polydispersity index (PDI) and the ζ potential. PDI is defined as

$$PDI = \frac{M_w}{M_n}, \tag{2.4}$$

where M_w and M_n are the weight average and number average molecular weight, respectively. PDI is the molecular weight distribution throughout the polymer, which composes the NPs stabilizing the MBs. [22]

The ζ potential is an abbreviation for electrokinetic potential in colloidal systems. It represents the surface charge of NPs and reflects their long-term stability. From a theoretical point of view, ζ potential is the electric potential in the interfacial double layer of a dispersed particle or droplet versus a point in the continuous phase away from the interface. In other words, ζ potential is the potential difference between the mobile dispersion medium and the stationary layer of the dispersion medium attached to the dispersed particle. pH of the medium is the most important factor affecting ζ potential, and other factors include ionic strength, concentration of any additives, and temperature. The significance of ζ potential is that its value can be related to the short- and long-term stability of emulsions. Emulsions with high ζ potential (absolute value) are electrically stabilized while emulsions with low ζ potentials tend to coagulate or flocculate, possibly leading to poor physical stability. In general, when the ζ potential of an emulsion is high, the repulsive forces exceed the attractive forces, resulting in a relatively stable system. This is favourable regarding MB stability in circulation. [23]

2.4 US-mediated delivery of NPs to tumours

Major efforts have been made in recent years to develop more effective systems for drug delivery to tumours, and many research groups concentrate around the combination of US and drug-loaded MBs. A schematic representation of some mechanisms by which energy deposition from FUS can enhance the delivery of drugs is shown in Fig. 2.3.

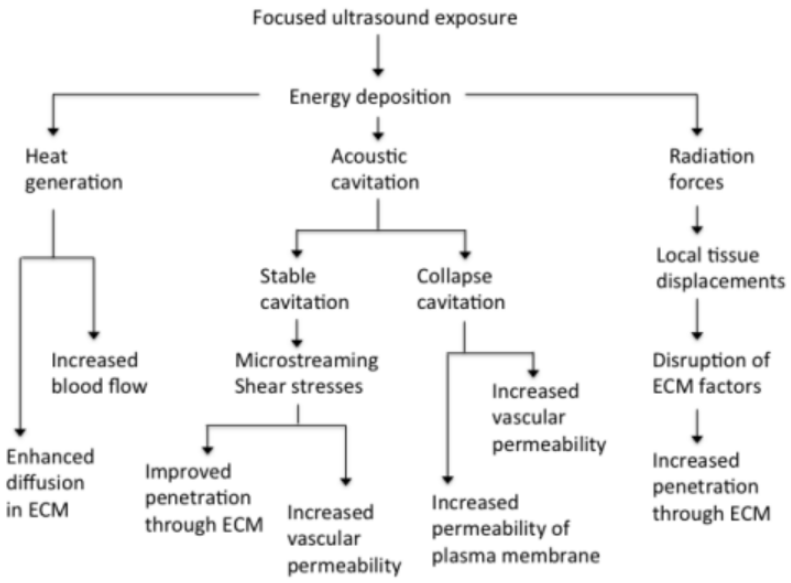

Figure 2.3: A schematic representation of various mechanisms by which energy deposition from FUS can enhance delivery of drugs. The figure is retrieved from Snipstad. [24]

2.4.1 Drug transport to tumours

For the drug to reach the cancer cells, two main obstacles need to be surpassed: the capillary wall, and the extracellular matrix (ECM).

The first step is getting across the capillary wall, and this is done by moving through the space between the endothelial cells which make up the outer layer. Fenestrated and sinusoidal capillaries have small holes or larger openings in the endothelium and membrane, making them easier for the drug to pass. These irregularities are among the reasons for the enhanced permeability and retention (EPR) effect seen in tumourous tissues, making the accumulation of the drug higher here than in normal tissues.

The next stage of infiltrating the cancer cells is for the drug particles to trespass the ECM, which provides physical support and protection for the cells. This transport is driven by diffusion and convection. Diffusion, being inversely correlated to molecular weight, makes drug transport a challenge. [9]

Intracellular uptake is also a big challenge, as the drug is seen as something foreign and attacked by various protective systems of the body, like endocytotic processing and degradation. [25]

2.4.2 Ultrasound mechanisms in improving drug delivery

US is believed to help drug delivery in several ways. Ultimately it provides energy to the place where it is applied, and this may lead to hyperthermia, cavitation and radiation forces that all improve drug delivery. Other advantages are its non-invasive nature, and the ability to penetrate deep into the body while still localizing its power very precisely. [26]

Local hyperthermia leads to enhanced diffusion in the ECM and increased blood flow, which is normally poor in the newly formed and immature capillaries in the tumour tissue. The acidotic and nutrient-deprived milieu here leaves the cancer cells with a higher thermosensitivity than normal cells, making them more powerless against additional treatment. [27]

US-mediated cavitation creates a negative pressure, making the gas bubbles oscillate. These oscillations produce microcurrents, shear stress and jet streams near the bubbles resulting in easier drug penetration through the capillary wall and the ECM, and increased drug release. One mechanism found by several groups, is that cavitation triggers the formation of temporary pores in the cell membrane, called sonoporation. [28]

Cavitation can be divided into two categories: stable and inertial cavitation. Stable cavitation mainly occurs at lower US intensities, while inertial cavitation is more normal for higher intensities. Inertial cavitation may finally lead to MB implosion, which will result in much stronger bioeffects. [29] Figure 2.4 illustrates the concepts of rarefaction and compression, displacements of molecules in a pressure wave, and stable and inertial cavitation of MBs. The bioeffects induced by cavitation are shown in Fig. 2.5, along with illustrations of microstreamings, shock waves, and jet streams.

Acoustic radiation forces occur when an US wave travelling through the tissue is absorbed or reflected by a particle, causing a momentum transfer from the US wave to the tissue. As a consequence, a steady flow called acoustic streaming drives the MB movement in one particular direction. The stream of MBs towards the vessel wall induces shear forces and may originate holes in the endothelium of the vessel wall, leading to improved delivery and distribution of NPs and drugs. [26]

To prevent unwanted bioeffects in diagnostic imaging, the upper limit of the MI is set to 1.9 to avoid induction of cavitation when MBs have not been introduced. [30]

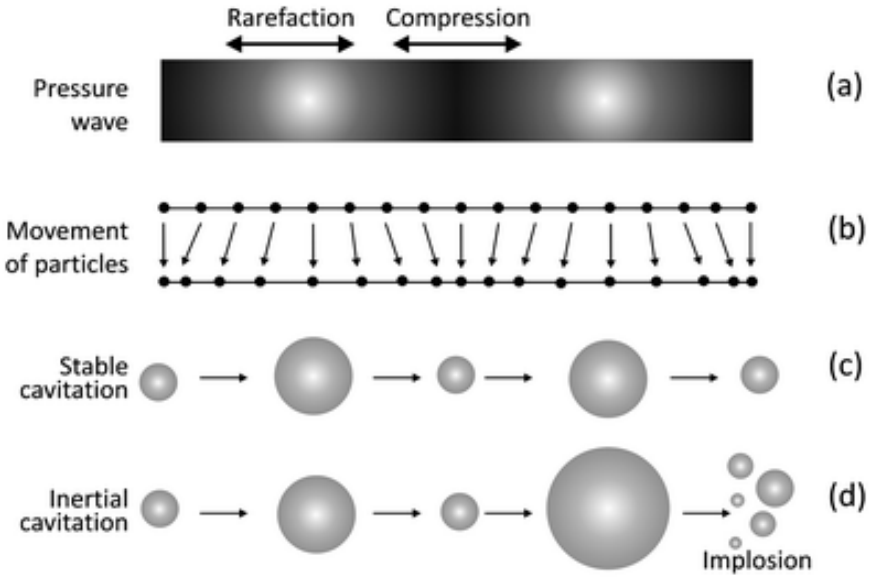

Figure 2.4: (a) Schematic representation of an acoustic pressure wave and (b) the displacement of molecules in a pressure wave. (c) and (d) show, respectively, stable and inertial cavitation of MBs. The figure is retrieved from Lentacker et al. [31]

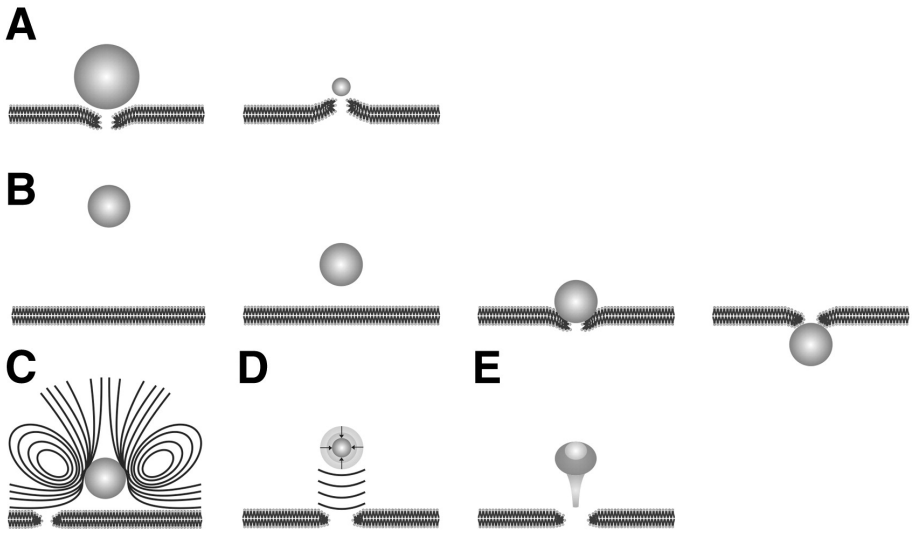

Figure 2.5: Bioeffects of stably and inertial cavitating MBs. (A), (B) and (C) refer to biophysical effects caused by stable cavitation, while (D) and (E) depict effects of inertial cavitation. (A) Pushing (left) and pulling (right) effects during the expansion and compression phase, respectively, of a stably oscillating microbubble, thereby disturbing the membrane integrity. (B) Acoustic radiation force causes microbubble displacement and compresses the microbubble against the cell membrane resulting in membrane disruption. The microbubble may even be pushed through the lipid bilayer to enter the cell. (C) Stable oscillation of a microbubble creates microstreamings in the surrounding fluid, which exert mechanical stress on the cell membrane, causing pore formation. (D) Shock waves produced by microbubble collapse generate high stresses on cell membranes, which results in membrane disruption. (E) When a microbubble collapses near a surface, the collapse is asymmetrical, leading to the formation of a liquid jet towards the surface. This microjet punctures the cell membrane, thereby creating a pore. The figure is retrieved from Lentacker et al. [29]

2.4.3 Ultrasound-mediated drug delivery

Relying on diffusion alone results in the disappointing 0.001 % of the drug dose reaching the cancer cells. [3] A more effective way is by developing DDSs that target the tumour more directly. The use of NPs as drug carriers is beneficial because they are too big to permeate blood vessels in healthy tissue, sparing normal cells from the drug. Utilizing the EPR effect in tumourous tissues lets the NPs seep through and thus affecting the cancer cells specifically at a much higher rate. However, overcoming the microvasculature is not enough, as this only harms the cells closest to the blood vessels and not the ones further into the tumour. To get the best possible effect of the treatment, reaching more tumour cells is required. Using MBs and US helps with this, and the basic concepts are illustrated in Fig. 2.6. The NPMBs carry drugs through the blood vessels of the patient. Insonation at the tumour site makes the affected MBs oscillate and ultimately explode, releasing the drug locally.

Moreover, the vibrations created by the US and the added flow from the drug release, help massage the blood vessels and tissues surrounding the tumour. Consequently, more pores are generated in the blood vessel walls enabling the drug to be pushed further into the tumour tissue. This system of exploiting NPs, MBs and US has proven to increase the drug dose delivered to the tumour by a total of 250 times, compared to conventional chemotherapy alone. Additionally, it has fewer side effects and also a lower risk of having to stop the treatment due to the general weakening of the patient's body. [4]

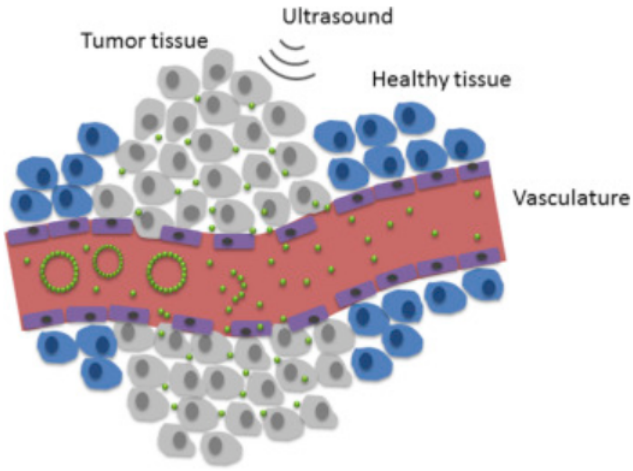

Figure 2.6: Illustration of how US and NPMBs can be used in targeted drug delivery. The MBs stabilized by NPs in green travel through the blood vessel from the left to right. Tumour cells are illustrated in grey, healthy cells are blue. Gaps between the purple endothelial cells are seen in the vicinity of tumourous tissues. US is focused at the tumour, releasing the drugs locally. The figure is retrieved from Snipstad et al. [32]

2.4.4 Sonoporation and sonopermeation

The term "sonoporation" has traditionally been used for refering to various effects caused by insonation, but in a recently published review article by Snipstad et al. it is proposed to be used exclusively when discussing the formation of temporary pores in the cell membrane.
"Sonopermeation" is recommended as a more collective term to capture the variety of effects caused by the combination of US and MBs in improved drug delivery. In addition to the opening of pores, other effects are opening of intercellular (tight) junctions, macroscopic changes in perfusion, changes in the perivascular and extracellular space, and stimulated endocytosis, transcytosis and/or exocytosis. [33]

2.5 Tumour cells for this study

To be able to study tumourous vasculature the CAMs were inoculated with OHS cancer cells. These were from an osteosarcoma cell line established from a patient with multiple skeletal manifestations of osteosarcoma, developing after bilateral retinoblastoma. The tumour cells expressed sarcoma-associated antigens and showed rapid growth in monolayers and as multicellular spheroids. They formed distinct colonies in soft agar, and subcutaneous tumours in nude mice. Morphological studies indicated that OHS cells had retained important characteristics of the cells of origin. Fodstad et al. [34] cultured the cells in agar-coated flasks, and saw that they rapidly formed growing multicellular spheroids. As seen in Fig. 2.7, the fast-growing spheroids reached the maximum volume 17 days after aggregation, $17 \cdot 10^6 \pm 1 \cdot 10^6$ μm^3 (mean $\pm$ SE), with a diameter of 319 ± 24 μm. The doubling time during the rapid growth phase was found to be approximately 1.5 days. After day 17 the mean spheroid size decreased.

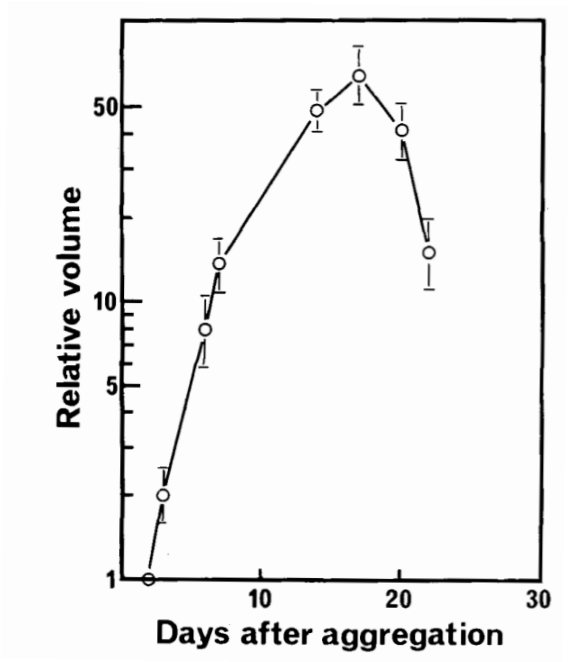

Figure 2.7: Growth curve for OHS multicellular spheroids cultivated in agar-coated flasks. The relative volume was calculated as the ratio between the average volume of 40 spheroids at the time of assessment, and the average volume of 40 aggregates measured shortly after the aggregation procedure. The figure is retrieved from Fodstad et al. [34]

2.6 The chorioallantoic membrane model

The chorioallantoic membrane (CAM) is a vascular fetal membrane in eggs of some amniotes, like birds and reptiles. It is composed of the fused chorion and the adjacent wall of the allantois, and is crucial to the development of the fetus. One of its tasks is the transportation of gases such as oxygen to the embryo. Another of its functions is delivering calcium from the eggshell to facilitate the bone formation of the growing embryo. [35]

The CAM is gaining popularity in biological and biomedical research as a model to study features like fetal development, angiogenesis, and tumours. For this work CAMs from chickens were developed to investigate drug delivery to tumours through the vasculature. The CAM is let to develop on top of a shell-less chicken embryo grown *ex ovo*. The intricate structure of the CAM vasculature is shown in Fig. 2.8, imaged in a stereo microscope. Figure 2.9 shows embryo and CAM development at embryonic days 3, 8, 10 and 14.

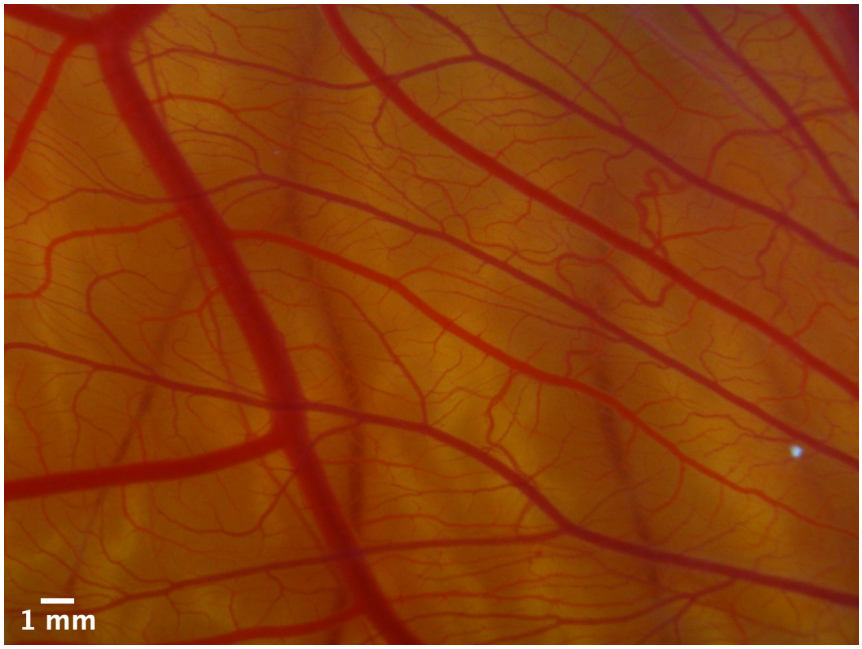

Figure 2.8: A stereo image of the intricate vasculature structure of a CAM grown *ex ovo*.

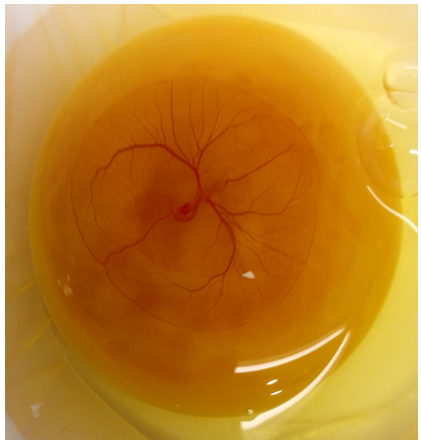

(a) Embryonic day 3.

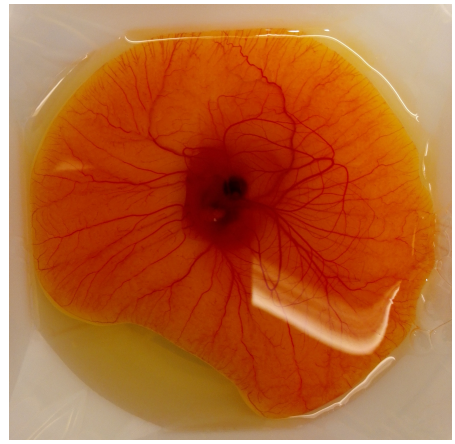

(b) Embryonic day 8.

(c) Embryonic day 10.

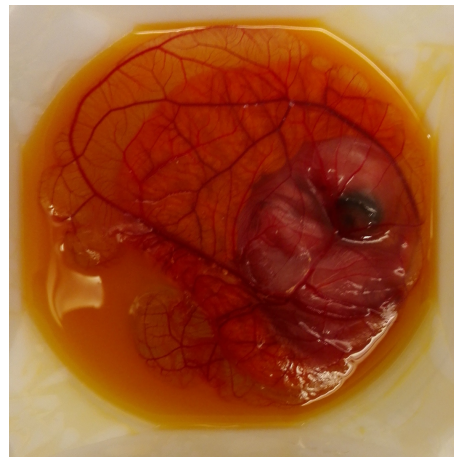

(d) Embryonic day 14.

Figure 2.9: Chicken embryo and CAM development at different embryonic days. The black spot is the eye, and the head, neck and body eventually curl around it. (a), (b), (c) and (d) show how the culture looks on embryonic day 3, 8, 10 and 14, respectively.

2.7 Epi-fluorescent microscopy

Fluorescence is the emission of photons by atoms or molecules whose electrons are transiently stimulated to a higher excitation state by radiant energy from an outside source. With light microscope optics adjusted for fluorescence microscopy, it is possible to examine the distribution of a single molecular species in a specimen. Under specialized conditions it can even detect specific, individual fluorescent molecules that fluoresce in the presence of excitatory light. Thus, the amount, intracellular location, and movement of macromolecules, small metabolites, and ions can be studied. Typically, non-fluorescent molecules are tagged with a fluorescent dye or fluorochrome in order to make them visible, and different molecules or particles can be given different tags. Since they can be distinguished from each other, it is possible to investigate both their individual and combined dynamics. The microscope contains special filters and employs a unique method of illumination to produce images of fluorescent light emitted from the excited molecules of interest.

The fluorescence microscope is modified in several important ways in order to obtain images that are bright and well defined:

- A bright light source, such as a mercury, xenon, or metal halide arc lamp, is required because only a narrow band of wavelengths, and consequently a small portion of the illuminator output, is used to excite fluorophores in the specimen.
- For efficient high contrast imaging, both the illuminator and objective are positioned on the same side of the microscope slide as the specimen. In this arrangement, the lamp and light delivery assembly are called an epi-illuminator, and the objective functions both as the condenser delivering excitatory light to the specimen and as the objective imaging lens, collecting fluorescent light and forming an image of the fluorescent object in the image plane.
- Fluorescence filter sets contain three essential filters: excitation filter, dichromatic mirror, and emission filter. They are positioned in the optical path between the epi-illuminator and the objective, an arrangement shown in Fig. 2.10.
- High numerical aperture (NA), oil immersion objectives made of low-fluorescence glass are used to maximize light collection and provide the greatest possible resolution and contrast. [36]

Epi-illumination is made possible by the employment of a dichromatic mirror, which is mounted together with exciter and emission filters as a fluorescence filter set in a filter cube (or optical block) that is positioned along the optical axis. The first component, the excitation filter, selectively transmits a band of short wavelengths (relative to the fluorescence wavelengths) for exciting a specific fluorophore in the specimen. The second component, the dichromatic mirror, reflects the short wavelength excitation light toward the objective and specimen, while transmitting returning long-wave fluorescent light toward the detector. The dichromatic mirror also directs any excitation wavelengths reflected by the specimen back toward the exciter filter and illuminator. The third component is the emission filter, which transmits the band of fluorescence wavelengths while blocking any residual short excitation wavelengths. The fluorescent wavelengths then form an image on the eye or camera. [36]

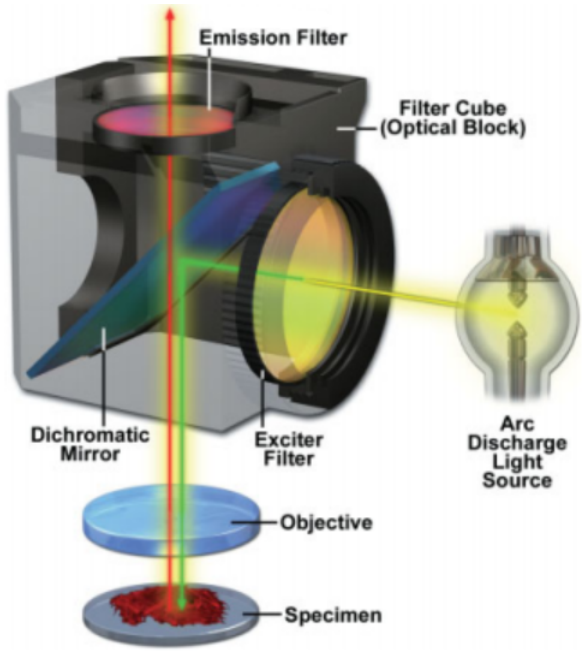

Figure 2.10: The orientation of filters in a filter cube in an epi-illuminator for an upright microscope. The excitation beam (yellow line) passes through the exciter and is reflected by the dichromatic mirror and directed toward the specimen (green line). The return beam of emitted fluorescence wavelengths (red line) passes through the dichromatic mirror and the emission filter to the eye or camera. Excitation wavelengths backreflected or scattered at the specimen are again reflected by the dichromatic mirror back toward the light source. Excitation wavelengths that manage to pass through the dichromatic mirror are blocked by the emission filter. The figure is retrieved from Murphy. [36]

2.8 Relevant research

To our knowledge, only two other external studies have currently been published about MBs and US-induced vascular effects in the CAM model, and these are summarized here.

In 2007, Stieger et al. [37] presented their work concerning the effects on lipid-shelled perfluroro-proprane-filled MBs injected into CAMs. The bubbles had a diameter of 1.8 ± 1.5 μm (mean $\pm$ SD) and were exposed to various MIs in the range of 0.5-2.4. The US waves were generated with one of two transducers: 1.00 or 2.25 MHz. The data acquired was divided into two categories: a low-stress class (MI < 1.13) and a high-stress class (MI > 1.3). Convective transport of the model drug was observed from micron-sized openings in the vessels walls. The authors found that the mean fluid velocities of the leading edge of dextrans were 188.6 μm/s and 362.5 μm/s for the low-stress class and the high-stress class, respectively. The threshold pressure for extravasation was 0.5 MPa for a transmitted center frequency of 1.00 MHz (MI = 0.5) and 1.6 MPa for a frequency of 2.25 MHz (MI = 1.06); thus, the frequency dependence of the threshold was not found to be predicted simply by the MI. They found effects of sonopermeation in vessels with a diameter of up to 55 μm, and the increased rate and volume of extravasation correlated with transmission pressure and decreasing centre frequency. Utilizing electron microscopy they saw micron-sized focal endothelial gaps and disseminated blebs, vacoules, and filopodia extending across tens of microns.

Ten years later, Tarapacki et al. [38] introduced their preliminary results on the effects of US and MBs (mean diameter: 1.1-3.3 μm) on blood flow and vascular architecture. The vascular bioeffects induced by combining US and MBs was found to increase with acoustic PNP. At 160 kPa, no visible differences were observed compared to the control. At 240 kPa, a transient decrease in perfusion with subsequent recovery within 15 min was observed, whereas at 320 kPa, the fluorescent images showed an irreversible vascular damage. The study indicated that a potential mechanism for the transient decrease in perfusion may be related to blood coagulation. The authors suggest that US and MBs can induce reversible and irreversible vascular changes depending on the acoustic pressure applied.

3 | Materials and methods

3.1 SINTEF nanoparticle-stabilized microbubbles

The SINTEF NPMBs utilized in this work are stabilized by NPs consisting of poly (2-ethyl-butyl cyanoacrylate) (PEBCA), a hydrophobic polymer. [32] Some of the characteristics of a typical NP batch are summarized in Table 3.1.

Table 3.1: Characteristics of a typical batch of NPs used to stabilize the MBs.

Particle batch	BBB2-29
Monomer	2-ethyl-butyl cyanoacrylate
PEG	Kolliphor HS15, Brij L23
Dye	NR668
Size (z-average)	160 nm
PDI	0.16
ζ potential	-3.7 mV

The NPMBs were provided by the Department of Biotechnology and Nanomedicine at SINTEF at the day of experiments. They were manufactured as described in "Ultrasound Improves the Delivery and Therapeutic Effect of Nanoparticle-Stabilized Microbubbles in Breast Cancer Xenografts" by Snipstad et al., 2017: "An oil phase consisting of 2-ethyl-butyl cyanoacrylate (monomer, Henkel Loctite, Düsseldorf, Germany) containing 0.1 wt% methane sulfonic acid (Sigma-Aldrich, St. Louis, MO, USA), 2 wt% Miglyol 812 (co-stabilizer, Cremer, Cincinnati, OH, USA) and 0.8 wt% azo bis-dimethyl valeronitrile (V65, oil-soluble radical initiator, Waco, Osaka, Japan) was prepared. Fluorescent particles for optical imaging were prepared by adding either NR668 (modified NileRed [39], custom synthesis, 0.5 wt%) or IR-780 Lipid (near-infrared dye, custom synthesis, CEA, Grenoble, France, 0.5 wt%) to the oil phase.

An aqueous phase consisting of 0.1 M HCl containing Brij L23 (10 mM, 23 PEG units, MW 1225, Sigma-Aldrich) and Kolliphor HS15 (10 mM, 15 PEG units, MW 960, Sigma-Aldrich) was added to the oil phase and immediately sonicated for 3 min on ice (6 x 30-s intervals, 60% amplitude, Branson Ultrasonics digital sonifier 450, Danbury, CT, USA). The solution was kept on magnetic stirring for 1 h at room temperature before adjusting the pH to 5 using 0.1 M NaOH. The polymerization was continued for 2 h at room temperature before increasing the temperature to 50 °C for 8 h while the solution was rotated

(15 rpm). The dispersion was dialyzed (Spectra/Por dialysis membrane MWCO 100,000 Da, Spectrum Labs, Rancho Dominguez, CA, USA) against 1 mM HCl to remove unreacted PEG. The dialysate was replaced three times. Details regarding PEGylation of the NP-platform have been published previously. [21; 40; 41] The size, PDI and ζ potential of the NPs were measured by dynamic light scattering using a Zetasizer Nano ZS (Malvern Instruments, Malvern, UK).

The NPMBs were prepared by self-assembly of the NPs (1 wt%, 10 mg/mL) at the gas-water interface by the addition of 0.5% casein in PBS and vigorous stirring using an Ultra-Turrax (T-25, IKAWerke, Staufen, Germany), as described. [21] Perfluoropropane (F2 Chemicals, Preston, Lancashire, UK) was used instead of air for increased circulation time. The average MB diameter, size distribution and concentration were determined using light microscopy and image analysis (ImageJ 1.48 v, National Institutes of Health, Bethesda, MA, USA). The NPMB solution is a combination of free NPs and NPMBs, where only a small percentage of the NPs are located on MBs." [32]

Previously, poly(butyl cyanoacrylate (PBCA) NPs were used before it was discovered that PEBCA NPs gave better properties for the purpose of drug delivery to tumours. [32] A longer and branched alkyl monomer chain was thought to be the reason for a slower degradation rate, which might give therapeutically favourable behaviours. [42; 43]

Figure 3.1 shows a vial of the NPMBs that were used in this study. The bubbles to be injected into the CAM were extracted from the darkest part of the solution, as the top part contains bubbles of perfluorocarbons.

Figure 3.1: A vial of the SINTEF NPMBs used in this study. The darker part at the bottom is NPMBs, while the lighter top part is bubbles of perfluorocarbons.

Characteristics of all the NPMB batches used for this work are shown in Table 3.2. Up to 8 micrographs were taken and analyzed for each batch. The number of micrographs used for each analysis and the results are given in the table, together with the purpose of each batch. A typical size distribution is given in Fig. 3.2, showing the analysis results of batch GB-598. Figure 3.3 shows one of the bright field micrographs taken of the NPMBs in this batch. The NPs are too small to be seen in a regular light microscope, but with a fluorescent filter they are visible as bright rings around the MBs as shown in Fig. 3.4.

The batches of NPMBs that were used in this study had an average diameter of 2.2 µm and an average concentration of $6.0 \cdot 10^8$ MBs/mL.

Table 3.2: Characteristics of all the batches of NPMBs used in this work. The concentration, average diameter and purpose is given for each batch. The fourth column gives the number of images which the analysis of MB concentration and average diameter is based on. For batch GB-607 images were not taken, but the NPMBs looked normal by visual inspection in the microscope.

Batch	**Concentration (MBs/mL)**	**Average diameter** (µm)	**Micrographs**	**Purpose**
GB-580	$6.22 \cdot 10^8$	2.20	8	US experiments
GB-583	$5.97 \cdot 10^8$	2.52	8	US experiments
GB-591	$6.61 \cdot 10^8$	1.92	1	US experiments
GB-598	$6.27 \cdot 10^8$	2.06	6	US experiments
GB-606	$5.73 \cdot 10^8$	2.26	8	Test of high speed camera
GB-607			Only visual inspection in microscope	Confocal imaging
GB-609	$5.31 \cdot 10^8$	2.26	8	US experiments

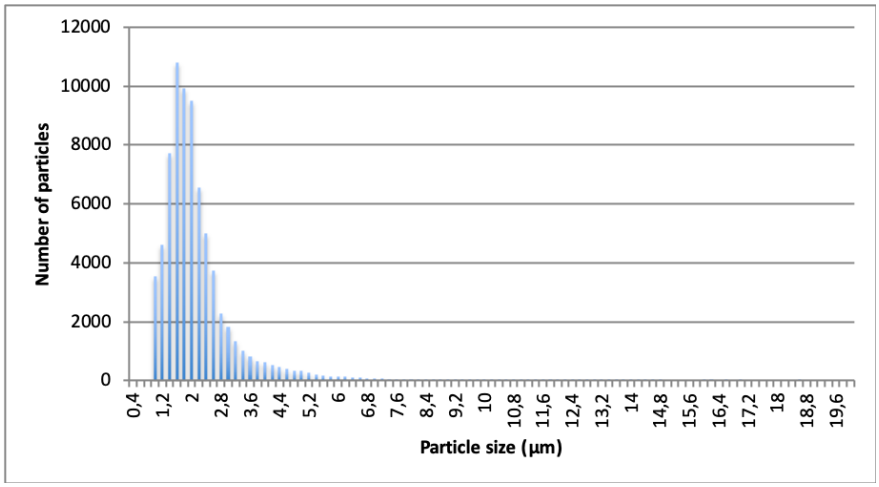

Figure 3.2: Size distribution of the NPMBs of batch GB-598.

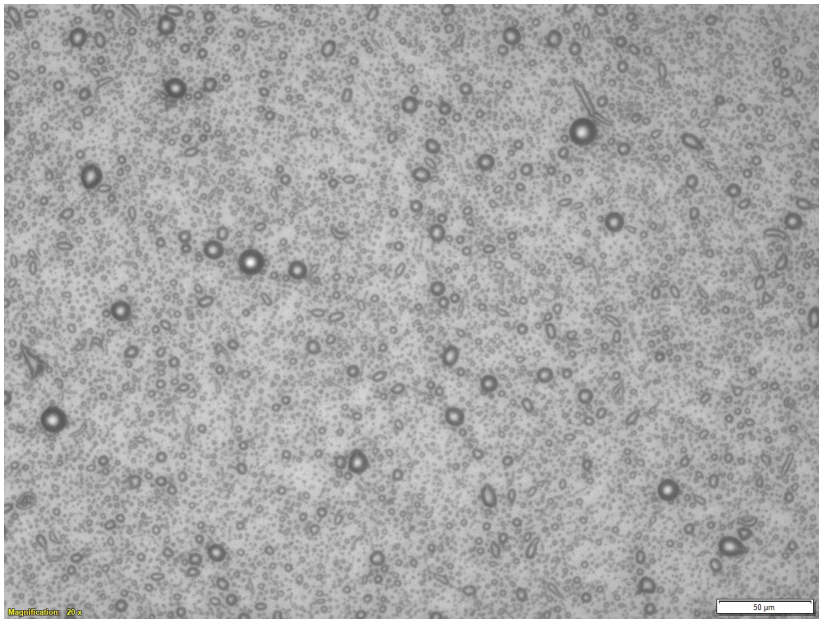

Figure 3.3: A bright field micrograph used to analyze the average concentration and diameter of the NPMBs of batch GB-598. A histogram of the size distribution is given in Fig. 3.2

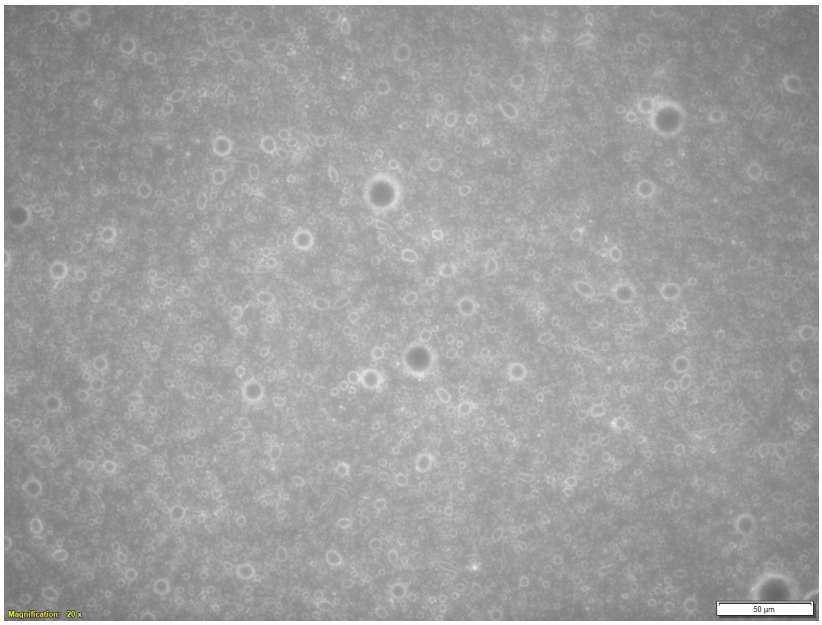

Figure 3.4: A fluorescent micrograph of the NPMBs of batch GB-598. The NPs are seen as bright rings around the MBs.

3.2 Cell culturing

OHS cells were cultured in RPMI-1640 medium (Life Technologies) with 10 % fetal bovine serum (Sigma-Aldrich) and 1 % penicillin-streptomyocin (Sigma-Aldrich). Penicillin-streptomyocin is an antibiotic and was added to avoid infections in the cell culture. Culturing was done in TC-75 flasks (VWR) and cell splitting was performed when the flasks were approaching 100 % confluence. $2 \cdot 10^6$ cells were put in each new flask and a new splitting was done four days later, expecting $16 \cdot 10^6$ cells. Cells normally spend one day adjusting to their new environment and attaching to the bottom of the flask, before they start growing exponentially. The cell splitting procedure was executed in a laminar air flow bench, following basic principles for sterile technique. First the growth medium was removed and 5 mL of phosphate-buffered saline (PBS) (Sigma-Aldrich) was added to the flask. It was tilted a couple of times to wash all the cells, then the PBS was removed. 3 mL trypsin (Sigma-Aldrich) was added to make the cells round up and detach from the bottom. Approximately 5 min in room temperature was usually sufficient, and 7 mL growth medium was added to stop the trypsin activity. If the trypsinization lasts for too long it can harm the cells, as trypsin hydrolyzes proteins. The cells and medium were gently resuspended with a pipette, before it was put in a 14 mL centrifuge tube. The suspension was centrifuged (Heraeus Megafuge 1.0) at 1500 rpm for 5 min. In the meantime, a few drops of cell suspension was put in a Bürker chamber and counted using a microscope (Leica DMIL). After centrifugation, the supernatant was removed and new medium was added so as the concentration was $1 \cdot 10^6$ cells per mL suspension. It was pipetted to a new flask together with fresh growth medium and put for incubation (Binder CB-150 climate chamber) at 37 °C with 5 % CO_2. PBS, trypsin and OHS growth medium were all heated to 37 °C prior to the splitting.

3.3 Preparation of the chick *ex ovo* culture

A timeline of the whole chick *ex ovo* culture preparation and US experiment is shown in Fig. 3.5 and explained in the following sections. The day after incubation for each step of the process is given below the line.

Figure 3.5: Timeline of the CAM model experiment, with the day after incubation given below the line. On day 3 the eggs were cracked and on day 6 they were inoculated with OHS cancer cells. The cultures were let to develop until day 13 and US experiments were performed.

3.3.1 Incubation

Fertilized chicken eggs were provided by Nortura SA. 30-50 eggs were wiped with a dry paper towel and incubated in an egg incubator (vidaXL) for three days. The incubator was set to 37 °C and 60-80 % humidity, to ensure optimal development conditions.

3.3.2 Cracking the eggs

On day three, the eggs were cracked open into polystyrene weighing boats (Globe Scientific) to create the *ex ovo* cultures. The cracking was performed in a sterile bench (Holten LaminAir), but the ventilation was turned off to prevent the egg content from drying. Three stacked weighing boats were used for each egg. The bottom one was whole, while the two on top were bottomless with a thin plastic foil in between as shown in Fig. 3.6. All parts were thoroughly sterilized with 70% EtOH before assembly.

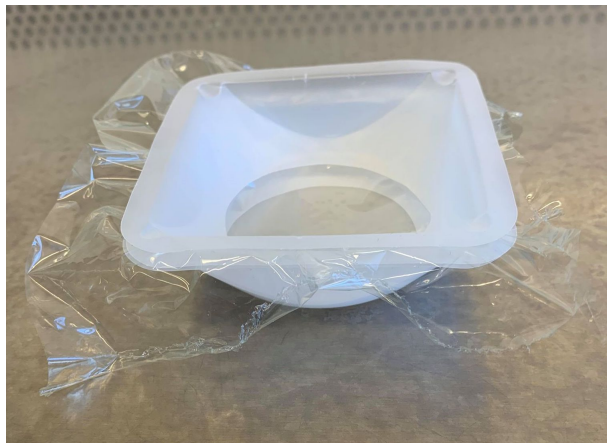

Figure 3.6: A weighing boat complex used to grow chicken embryos *ex ovo*. Two weighing boats with the bottom cut out have a piece of plastic foil between them, and are placed in a third weighing boat.

One egg at the time was taken out of the egg incubator, wiped with 70% EtOH and cracked. The eggs were cracked open by knocking it gently against a 80 mm triangular magnetic stir bar, opened and then let to flow straight into the weighing boat complex. The whole process must be done carefully, to prevent the yolk membrane from rupturing. The complex was then placed in a Petri dish (Sigma-Aldrich) where the bottom had been covered with deionized water (DIW), and the lid was placed on top of the complex. The cultures were incubated (Thermo Electron Corporation) at 37 °C, the CO_2 supply turned off, and with a water tray in the bottom to maintain the humidity.

3.3.3 Inoculation

On day six the cultures were inoculated with OHS cells. The cell harvesting followed the same procedure as cell splitting up until the supernatant was removed after centrifugation. OHS growth medium and ECM gel (Sigma-Aldrich) was added in equal amounts to reach a concentration of 10^5 cells per µL. From the cutout weighing boat bottoms, rings of inner diameter 5 mm were made with a hole punch and a pair of scissors. Using a sterilized pair of tweezers a small area of the CAM surface was scratched and a ring placed over it. The scratching was done to traumatize the CAM, in order to facilitate the processes of cell inoculation and angiogenesis. 35 µL of cell suspension was put in the middle of the ring using a cold pipette. 35 µL of cell suspension contains $1.75 \cdot 10^6$ cells with a 1:1 ratio between growth medium and ECM gel. The ECM gel is a mixture of gelatinous proteins, here used as a substrate for the cancer cells. It is retrieved from Engelbreth-Holm-Swarm sarcoma in mice and has a protein concentration of 8-12 mg/mL. It will gel after 5 min at 20 °C, so work should be done at temperatures below 10 °C. The pipette tips were therefore cold, being stored in the freezer prior to the procedure. During the inoculation, the tips and the cell suspension were stored on ice.

After inoculation, the culture was placed back into the incubator for further development. Figure 3.7 shows an *ex ovo* culture that has been inoculated with OHS cells, where the cells have been let to grow inside the ring. (a) shows the weighing boat with the culture, while (b) shows a close-up of the ring imaged in a stereo microscope.

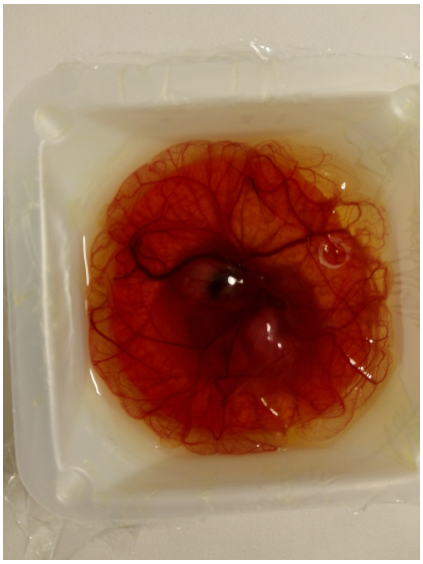

(a) An *ex ovo* culture inoculated with OHS cells. The cells are pipetted inside the white ring to the right of the embryo.

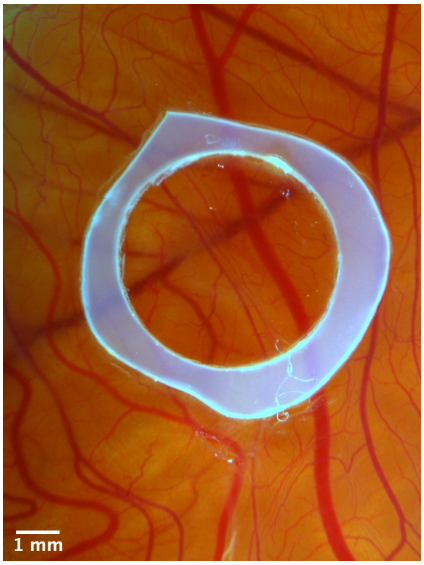

(b) A close-up image of the ring taken in a stereo microscope.

Figure 3.7: A CAM culture inoculated with OHS cells. The cells are pipetted inside the ring to the right in (a), and (b) shows a close-up of the ring.

3.4 Ultrasound experiments

On day 13 the experiments with NPMBs and US treatment were conducted, described in detail in the next sections. Fluorescently labelled 2 MDa dextrans were used to visualize the vasculature of the CAM during imaging. The dextrans are hydrophilic polysaccharides synthesized by bacteria. They are labelled with fluorescein isocyanate (FITC), which has an excitation maximum at 490 nm and an emission maximum at 520 nm. Their Stokes radius is 27 nm. [44] The SINTEF NPMBs were delivered at the day of experiments, and their detailed description can be found in Section 3.1.

3.4.1 Injection

The cultures were transported in a polystyrene box to the microscopy room, where they were kept on a heating pad (Wilfa) during the duration of experiment preparation. To minimize muscle contractions during imaging the embryo was sedated prior to the experiment by applying 300 µL of medetomidine (Domitor, Pfizer), diluted with PBS to 0.05 mg/mL, on top of it. This event marked the starting point of the experiment, as the medetomidine should be let to work for at least 10 min to achieve satisfactory sedation. Given that an egg weighs approximately 50 g, the applied dosage was 0.3 mg/kg.

Choosing an appropriate site of injection required some considerations. When possible veins were chosen over arteries, as they cause less bleeding. Both size and location of the vessel were also evaluated. It needed to be wide enough to place a catheter into it, but compromised by the fact that bigger vessels cause more bleeding. Extensive bleeding was unwanted because it could disturb the imaging and the embryo might die too early from loss of blood. Another aspect was the injection itself, as spillage of dextrans and/or NPMBs could disturb the images. Too much of either would cause a high degree of background in the images, which could make them impossible to analyze. The last thing taken into account was the placement of the catheter. It had to be in a suitable proximity to the wall of the weighing boat, as this is where it was attached. Additionally, it needed to be placed in such a way that it could cater a second injection. All these aspects combined, the site of injection was preferably a medium sized vein relatively close to the wall of the weighing boat but far from the site of imaging.

50 µL of dextrans were drawn into a 1 mL syringe (B. Braun). The same amount of NPMBs was drawn into a similar syringe. The dextrans had been diluted with PBS to a concentration of 10 mg/mL. The vial of NPMBs was rotated gently before extracting the NPMBs. Drawing NPMBs from the vial was done as carefully as possible to avoid destroying them. The change of pressure inside the vial was counteracted by inserting a cannula beside the other one. Wide cannulas were used (23G x 1" (Henke Sass Wolf)) to minimize the pressure forces acting on the NPMBs on their way through it.

Holding the vessel with a pair of tweezers, a catheter was inserted into it. For the first rounds of experiments 24GA 0.7 x 19 mm catheters (Becton Dickinson Infusion Therapy AB) were used, but later it was discovered that the slightly smaller 26GA 0.6 x 19 mm (Becton Dickinson Infusion Therapy AB) were better. The site of injection was glued with Super Glue Precision (Loctite), and the catheter was secured to the wall of the weighing boat with Micropore Surgical Tape (3M) as shown in Fig. 3.8. The bottom weighing boat of the complex was removed before injecting the dextrans, and the CAM was placed under the microscope. Imaging was started, the NPMBs were injected and US treatment initiated. After the imaging process described in Section 3.5.1, the embryo was sacrificed by decapitation using a pair of scissors.

Figure 3.8: The catheter was taped to the wall of the weighing boat during the experiments.

The concentrations were 5 mg dextrans/mL and $0.6 \cdot 10^9$ MBs/mL. In mice the blood volume depends on their body weight, averaging around 58.5 mL of blood per kg. If a mouse weighs 25 g, its blood volume will therefore be approximately 1.46 mL. [45] The blood volume of a chicken embryo reaches its peak around day 16-18, and its mean blood volume is 1.15 mL on day 12 and 2.15 mL on day 14. [46] As the US experiments were done on day 13, the blood volume of the embryo is comparable to that of a mouse. Thus, the concentrations injected in the chicken embryos can be compared to those used in mice. Mouse dorsal window experiments with SINTEF NPMBs subjected to US will be discussed later.

In the specialization project dextrans and NPMBs were co-injected with a regular syringe as shown in Fig. 3.9. Consecutive improvements were done to the method in this work, and catheterizing the blood vessel proved to have several advantages. Among them was saving time from NPMB injection to imaging, as the NPMBs have a rapidly decreas-

ing circulation time. Moving the culture to the microscope, finding a suitable imaging site and adjusting the focus usually takes several minutes, in which a substantial part of the NPMBs are already cleared from the circulation. Figure 3.10 shows how the concentration of NPMBs decreases rapidly with time. The analysis is performed in mice, but is probably similar in the CAM.

Figure 3.9: Co-injection of dextrans and NPMBs into a vein of the CAM, as it was performed in the specialization project. In this work, a catheter and serial injection of dextrans and NPMBs were utilized instead.

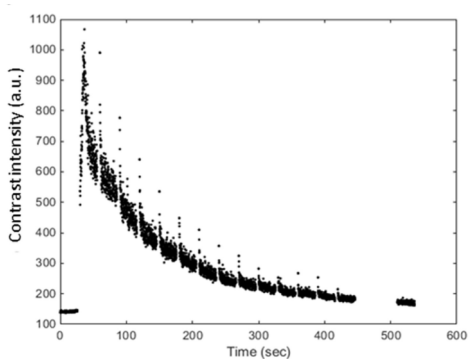

Figure 3.10: Circulation of the NPMBs in mice. Contrast intensity was quantified and is shown as a function of time to illustrate the time scale at which MBs are present in circulation. The graph is retrieved from Snipstad et al. [32]

3.5 Microscopy and ultrasound set-up

The CAMs were imaged using a Leica DM6 FS microscope, a Leica DFC7000 T colour camera, and the LAS X software (all by Leica Microsystems). The epi-fluorescent microscope had a mercury metal halide as a light source. A HC PL FLUOTAR 4x/0.13 objective (Leica) was used, giving a total magnification of 40x. The GnR filter cube (Leica) was utilized to visualize both the dextrans and the NPs, as it has a dual emission filter. It has an excitation filter of 450-490 nm, and two emission filters: The one of 500-550 nm visualized the dextrans, while the one of 600-670 nm visualized the NPs.

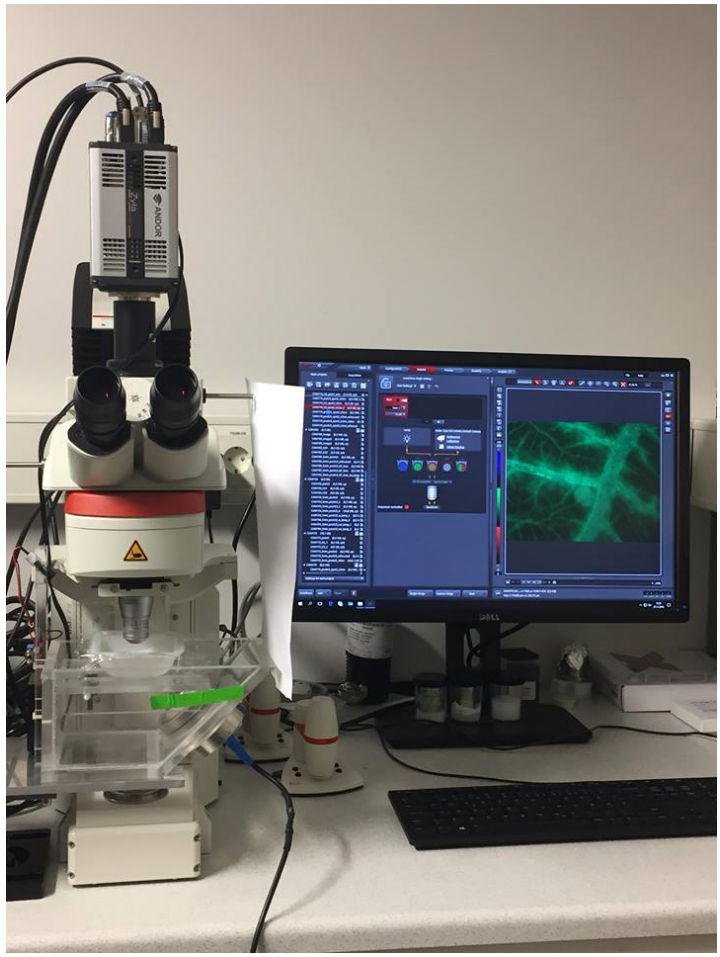

Figure 3.11: Parts of the experimental set-up. The CAM is placed on top of the water chamber and imaged from above by an epi-fluorescent microscope. An image obtained can be seen on the computer screen to the right, with the blood vessels clearly visualized by dextrans in green.

Figure 3.11 illustrates parts of the US experiment set-up. The CAM was placed on top of a custom made plastic water chamber designed by Andreas Åslund and made by "Finmekanisk verksted" at NTNU. This chamber let the CAM be insonified from below at an angel of 45° while imaging from above. A hole in the top plate let the US pass through to the CAM. One side of the chamber was tilted 45° and had a hole where the transducer was placed. The chamber was filled with degassed water, so that the water was in contact with the plastic foil of the weighing boat complex. A small laser diode was attached to the chamber, so that the US focus area could be aligned with the imaging. The set-up and settings were done so that the CAM would be in US focus. To generate the US signal, a waveform generator (33500, Agilent) and a 50 dB amplifier (2100 L, Electronic Navigation Industries) were used. The 1 MHz ultrasonic transducer (Precision Acoustics) had a diameter of of 60 mm and a focal distance of 73 mm. At the focus, the -3 dB beam width in both x and y directions was 2.2 mm. The US transducer had been characterized and calibrated in a water thank system to obtain the relation between input voltage and output acoustic power.

The US settings used to insonify the CAMs correspond to an MI of 0.4. The frequency was set to 1 MHz, the amplitude to 33.6 mVpp, and the burst period to 2 s and 10 000 cycles.

3.5.1 Epi-fluorescent imaging

The CAMs were treated with US and imaged either in cancerous vasculature inside the ring or in normal vessels if the ring was not accessible for imaging. A site above the yolk was always chosen. The exposure time was set to 100 ms, and a series of 1516 images were taken for each experiment. First a pre-image was taken, then video recording was started. The time of day for sedation, injections and imaging for each CAM were noted in the lab journal. 5-7 min of US treatment were recorded, and 10-30 s after turning it off were also included. Post-images of the treated area were taken for up to 30 min after US exposure.

3.5.2 Image analysis

Image analysis was done using the Fiji version of ImageJ (National Institutes of Health, Bethesda, MA, USA), an image processing program. Representative stacks were made for each series of images, and analyzed for the degree of extravasation and the size of blood vessels. Extravasation was studied by measuring the mean intensity inside ROIs close to a vessel, both in the green and the red channel. They represent the dextrans and NPs, respectively. Additionally, for one experiment that gave clearly visible extravasation, preliminary analyses were done to study the distance in which extravasated material could travel into the surrounding tissue.

4 Results

4.1 The *ex ovo* cultures

A total of 250 eggs were incubated and 170 of them successfully cracked. Inoculation was performed on 87 CAMs, with one, two or three rings of OHS cells. 46 cultures developed until day 13 and were used in experiments. Accumulated death rate by day after cracking was not found to be relevant for the scope of this thesis, and therefore a thorough analysis of it was not conducted. However, it is assumed to be similar to the results obtained in the specialization project, which is shown in in Fig. 4.1. [47]

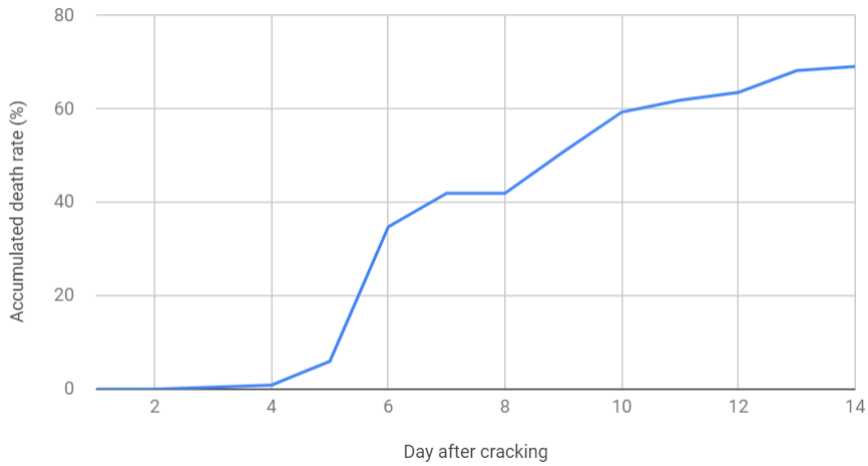

Figure 4.1: Accumulated death rate of *ex ovo* cultures by day after cracking. The figure is retrieved from the specialization project report. [47]

4.2 Ultrasound experiments with nanoparticle-stabilized microbubbles

9 CAMs were successfully serially injected with dextrans and NPMBs, and imaged by an epi-fluorescent microscope. Additionally 1 CAM was used solely as a control without NPMBs, but also some of the others were imaged prior to the injection of NPMBs. In total, 18 unique experiments were performed and their parameters are presented in Table 4.1. An X indicates that NPMBs were injected, which was the case for most of the CAMs. The use of US treatment was also true for the majority of them. All of the CAM cultures had been inoculated with OHS cells a week prior to experiment, the tumour cells located inside 1-3 polystyrene rings. Disappointingly, nearly all the rings had moved to a place impossible to image. During the remaining period of culture development after inoculation, the rings had moved as the CAM grew. At the day of experiment, they were either on top of the embryo or outside the rim of the yolk. Therefore, all but two cultures were imaged outside the ring, where the vessels are presumably normal.

Table 4.1: All the successful experiments are shown here. An X indicates that NPMBs were injected, US was turned on or that it was imaged inside the ring with OHS cells. Close to all of CAMs had to be imaged outside the ring, in which healthy vasculature is assumed. Many of the CAMs were imaged at two different FOVs or with different parameters, giving multiple entries for some of them.

Experiment	NPMBs	US	Ring
1	X	X	-
2	X	X	-
3	X	X	-
4	X	X	-
5.1	X	X	-
5.2	X	X	-
6.1	X	X	-
6.2	X	X	-
7.1	-	X	X
7.2	X	X	X
7.3	X	X	-
8.1	X	-	-
8.2	X	X	-
9.1	X	-	-
9.2	X	X	-
10.1	-	-	X
10.2	-	-	X
10.3	-	X	X

4.2.1 Phenomena found by epi-flourescent imaging during insonation

Table 4.2 shows all the 16 phenomena found in this study. Only the 14 experiments where NPMBs were injected are included in the fractions. The phenomena are related to the behaviour of the NPMBs and the properties of the CAM vasculature, both with and without US treatment. The number of experiments in which it was seen is given, together with its total percentage and the share of US and non-US treated CAMs.

Table 4.2: All the phenomena found in this study are listed in this table. The fraction out of the 14 experiments in which is was seen is given, in addition to the total percentage, and whether the imaged area was insonated or not.

Fraction	Phenomenon	Total (%)	US (%)	No US (%)
1/14	Slow extravasation of dextrans/NPs from blood vessels	7	100	0
1/14	Burst extravasation of dextrans/NPMBs from blood vessels	7	100	0
6/14	Veil of NPs on top of the vasculature	43	50	50
3/14	Only a few visible aggregates of NPs	21	100	0
2/14	NP accumulation along walls of blood vessels	14	100	0
7/14	NP accumulation in small blood vessels	50	100	0
9/14	Vasoconstriction	64	100	0
1/14	Vasodilation followed by vasoconstriction	7	100	0
1/14	Hindered perfusion leading to NP accumulation	7	100	0
11/14	Changes in the direction of perfusion	79	82	18
1/14	Leaky blood vessels prior to US treatment	7	0	100
1/14	Dark spots along blood vessels prior to US treatment	7	0	100
2/14	Sudden perfusion of blood vessels	14	100	0
2/14	Red spots pre US	14	100	0
3/14	Tumourous vasculature outside the ring of cancer cells	21	100	0
1/14	NPMBs entering through one blood vessel	7	0	100

The results obtained from analyzing the most relevant phenomena are presented in the following sections. The three latter in Table 4.2 are not included, as these were found less interesting for the scope of this thesis.

All the images from epi-fluorescently imaged US experiments have had their settings altered during analysis, to be able to view the NPs.

The time runs from imaging is started, so t = 0 is before both injection of NPMBs and US exposure.

4.2.2 Extravasation of dextrans and nanoparticles

One CAM showed extravasation of dextrans and NPs from the imaged vasculature. See the attached Video 1. The events were classified into two types; slow extravasation and burst extravasation. Slow extravasation was characterized by a gradual movement of dextrans and NPs away from the blood vessel, while burst extravasations were of a more rapid nature, resembling vessel ruptures.

Figure 4.2 shows a selection of images of the extravasation events. The time of experiment is given for each of the subfigures (a)-(f). US treatment was initiated at t = 17 s. Slow extravasation is especially seen from the large vessel to the right, which has a diameter of 325 μm. The sites of burst extravasation are pointed out by arrows. The three burst extravasations to the left happen along a vessel with a diameter of about 60 μm. The vessel exhibiting burst extravasations to the right has a diameter of approximately 40 μm.

All the burst extravasations took place at or close to vascular branching points where NP aggregates had accumulated. The aggregates can also be seen in the figure, particularly the large one appearing in in (b), shortly after US treatment was started.

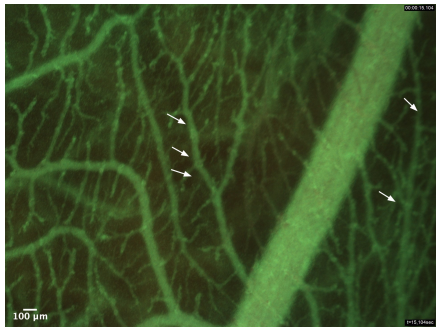

(a) Before US treatment, t = 15 s.
The arrows point to where the five burst extravasations later appeared.

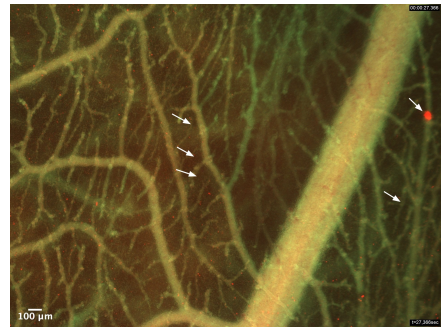

(b) 10 s into US treatment, t = 27 s.
A large aggregate of NP appears to the right.

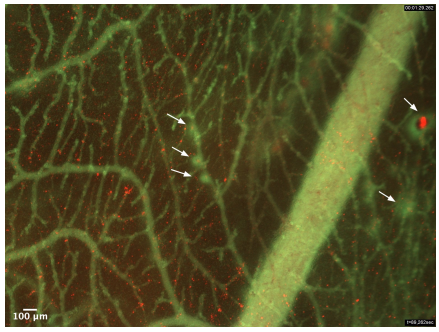

(c) 72 s into US treatment, t = 89 s.
The five sites of burst extravasation are shown by arrows.

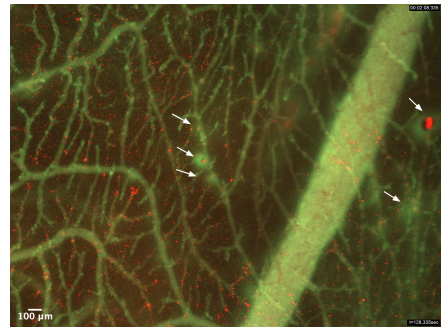

(d) 111 s into US treatment, t = 128 s.
Signs of slow extravasation from the large vessel are starting to show.

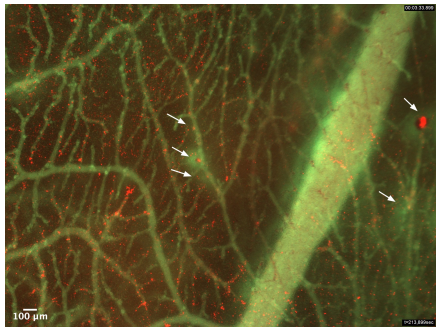

(e) 197 s into US treatment, t = 214 s.
Material is slowly extravasating from the large vessel.

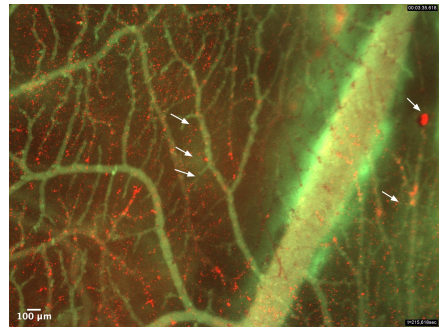

(f) End of 7 min of US treatment, t = 432 s.
Slow extravasation is seen from the widest vessel, its diameter is 325 µm.

Figure 4.2: An US experiment showing events of both slow and burst extravasation from the vessels. (a)-(f) show a selection of images from the series, and the corresponding times of experiment are given below each image. Arrows point to the five sites of burst extravasation identified. US treatment was started at t = 17 s. The large vessel exhibiting slow extravasation has a diameter of 325 µm.

A stack of 17 images from the experiment was analyzed in Fiji and the chosen regions of interest (ROIs) are presented in Fig. 4.3. The ROIs gave the plots in Fig. 4.4a and Fig. 4.4b, for the channel for dextrans and NPs, respectively.

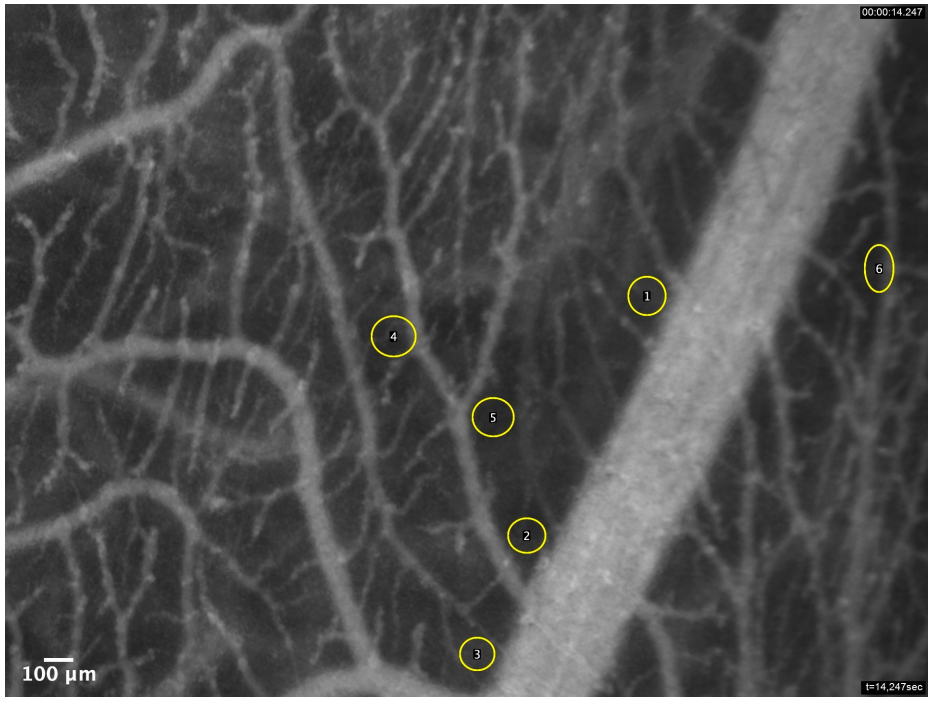

Figure 4.3: The ROIs analyzed for the US-treated vessels shown in Fig. 4.2. ROI 1-3 measured slow extravasation along a blood vessel with a diameter of 325 µm. ROI 4 measured the burst from a 60 µm thick vessel. ROI 6 investigates the largest burst, from a 40 µm thick vessel. All the burst extravasations originated from sites of NP aggregation at or close to a branching point. ROI 5 is located below a branching point. It was initially placed to investigate the background signal, as it portrayed the least degree of intensity changes.

Figure 4.4 shows the results from the analysis. (a) shows the increase of mean intensity of dextrans measured inside each ROI, while (b) shows the same for the NPs. Slow extravasation (ROI 1-3 and 5) is gradual, while burst extravasation (ROI 4 and 6) is of a more rapid, explosive nature.

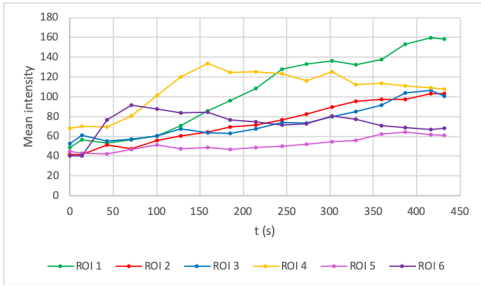

(a) Mean intensity over time measured in the green channel, showing slow extravasation and burst extravasation of dextrans.

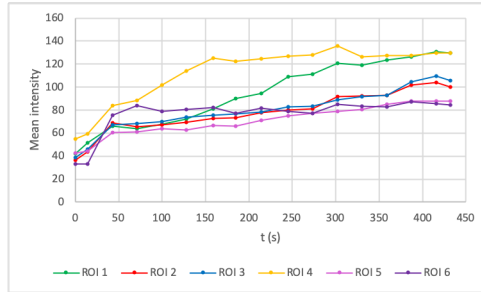

(b) Mean intensity over time measured in the red channel, showing slow extravasation and burst extravasation of NPs.

Figure 4.4: Mean intensity as a function of time in US-treated CAM vasculature, inside the ROIs shown in Fig. 4.3. (a) is the analysis for the dextrans channel and (b) is for the NP channel. ROI 1-3 was placed to measure slow extravasation, while the purpose of ROI 4 and 6 was to study burst extravasation. All the burst extravasations originated from sites of NP aggregates at or close to a branching point. ROI 5 shows, as intended, barely no change in the mean intensity for the dextrans. Surprisingly, the NPs still seem to have extravasated at the same rate as in the other ROIs.

The mean distances in which the extravasated material traveled from the 325 µm blood vessel are graphed in Fig. 4.5. The front of traveling dextrans and NPs were tracked to see how far into the surrounding tissue they are able to penetrate. They seem to travel at the same pace and reach to the same location, approximately 300 µm away from the blood vessel they extravasated from.

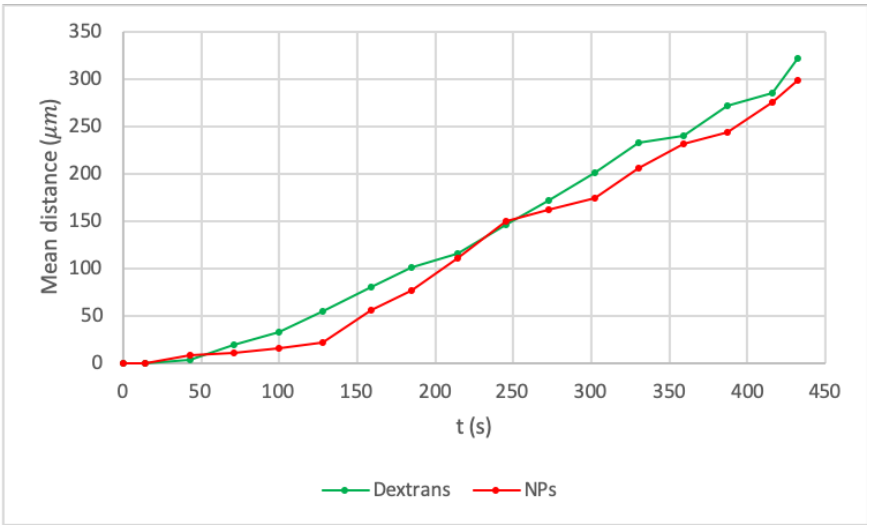

Figure 4.5: The mean distance as a function of time in which extravasated material traveled from a 325 µm thick blood vessel exposed to US treatment. The green line shows the movement of dextrans, while the red shows the same for the NPs. Insonation was initiated at t = 17 s and lasted about 7 min.

4.2.3 Accumulation of nanoparticles

Four patterns of NP accumulation in CAM vasculatures were observed in this study. 43 % presented an apparent veil of NP aggregates overlaying essentially the whole vasculature, while 21 % of the CAMs had only a few (1-5) NP aggregates visible in the FOV. A high degree av NP accumulation was observed along the blood vessel walls in 14 % of the CAMs, whereas a total of 50 % showed NPs particularly located to smaller vessels. All these phenomena presented themselves solely in experiments that included US treatment, except the NP veil, which was observed just as often in non-insonated vasculatures as in US-exposed ones.

It is unknown why the CAMs portray such different NP accumulation patterns, but it may be due to variable vessel properties between the CAM cultures. A quite extreme case of vessel leakiness is shown in Fig. 4.20, which can be contrasted to a more normal outlook for instance presented in Fig. 4.7.

Another observation relating to NP accumulation was a CAM which revealed a high degree of NP accumulation at a site of hindered blood perfusion. The reason for the impeded perfusion is unknown, but is thought to be connected to the total experiment time span for this particular CAM culture leading to a decreased perfusion rate. The following sections describe these five phenomena related to NP accumulation in more detail, and present the results obtained from analyzing the series of images taken.

Apparent veil of nanoparticles on top of the imaged vasculature

The feature of a semi-random NP veil apparently overlaying the imaged vasculature, instead of following the blood vessels, was observed in numerous CAMs. At the sites where the NPs accumulated, a gradual build-up was observed during the experiment. Free NP aggregates flowed into the FOV, but most of them were quickly immobilized at sites already inhabited by other aggregates.

The phenomenon was found to be more apparent in normal vessels compared to tumourous ones, 5/14 and 1/14 CAMs, respectively. Furthermore, it was seen both with and without the presence of US exposure. This may imply that a fairly continuous distribution of NP aggregates is associated with the properties and interactions between the NPMBs and the vasculature, and not a consequence of sonication. However, considering the minimal number of data points in this study these findings are solely a suggestion for further studies.

An example of the NP veil phenomenon is shown in Fig. 4.6. The FOV was the second one imaged for this CAM culture, and a second dose of NPMBs was injected prior to US treatment. For the image shown, insonation had not been initiated yet.

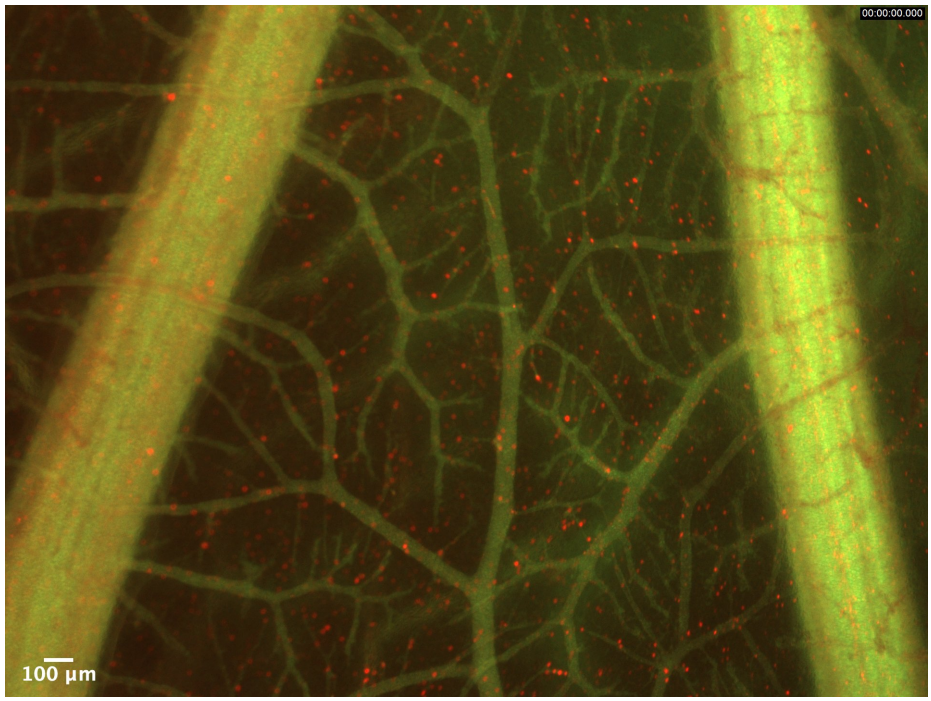

Figure 4.6: A CAM showing the apparent veil of NP aggregates covering the vasculature. A second dose of NPMBs had been administered at this point in the experiment, but US exposure had not been applied.

Accumulation of only a few aggregates of nanoparticles

For three experiments only a few (1-5) aggregates of NPs were seen in the FOV after US treatment. Figure 4.7 shows an image from one of these experiments, with the NP aggregate pointed to by an arrow. The aggregate is barely visible, even though the settings are the same as for the other images in this thesis. After careful considerations it was confirmed that the aggregate was only detectable in the red fluorescent channel, indicating a successful injection of NPMBs. The signal it produced grew gradually stronger up until this time point of the experiment, then it faded. The image shown is from t = 170 s in the imaging process, US treatment was initiated at t = 31 s. The two other NP aggregates present in this CAM appearing after the one shown had faded. The attached Video 4 shows the recording of this CAM.

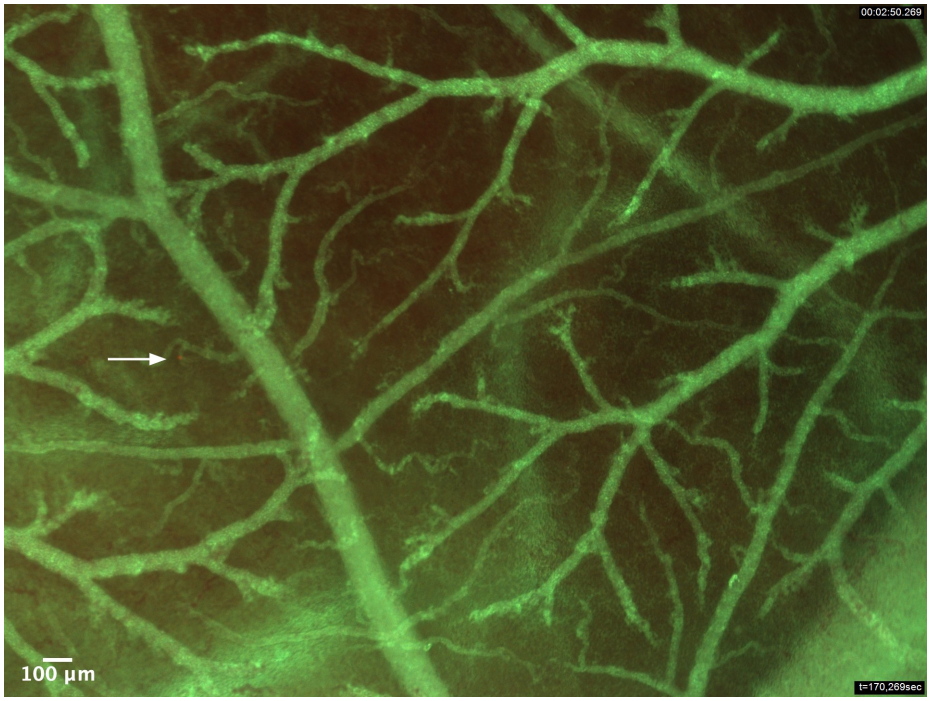

Figure 4.7: A CAM that showed accumulation of just three NP aggregates. An arrow points to a barely visible NP aggregate. The image is taken at t = 170 s, 139 s after US exposure was started. The settings are the same as for the other images, highlighting how weak the NP signal is.

All the CAMs where NPMB batch GB-580 were administered presented the same phenomenon of scarcely any NPs present. It was therefore suspected that this oddity was caused by a flaw in these particular NPMBs, but according to the producer the micrographs and the analysis results looked normal compared to the other batches.

Three ROIs for this experiment were analyzed for the mean intensity of both dextrans and NPs separately. The ROIs used are shown in Fig. 4.8 and the results are graphed in Fig. 4.9. The diameter of the vessels closest and perpendicular to ROI 1, 2 and 3 are 55 µm, 80 µm, and 97 µm, respectively.

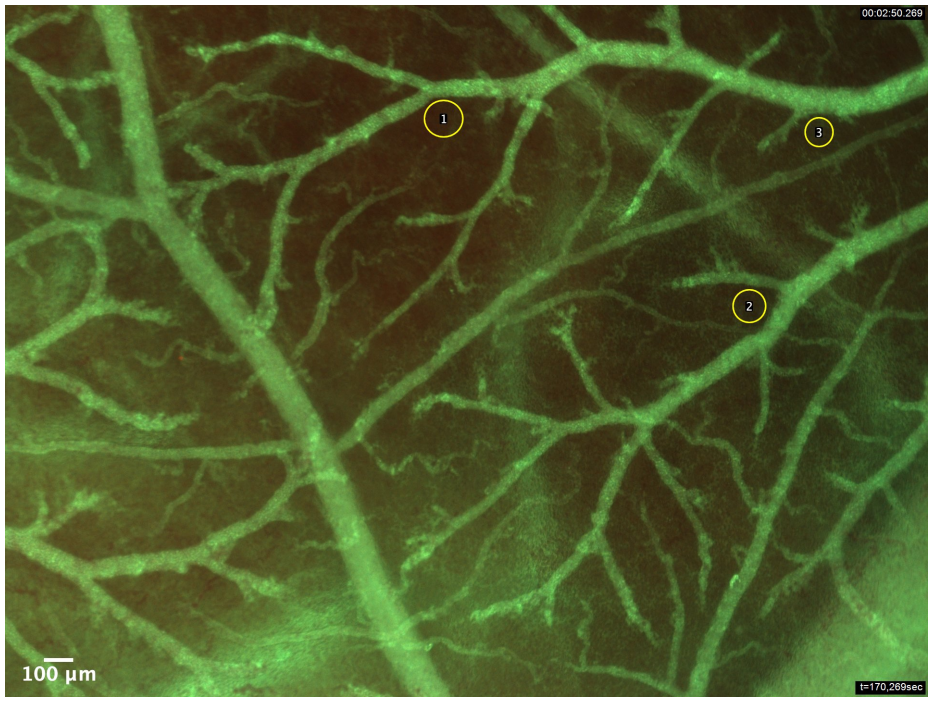

Figure 4.8: The ROIs used to analyze a CAM presenting only a few aggregates of NPs. The diameter of the vessels perpendicular to ROI 1, 2 and 3 are 55 µm, 80 µm, and 97 µm, respectively. The mean intensities over time for these ROIs are plotted in Fig. 4.9.

The intensities remained more or less constant during the experiment, for both the dextrans in Fig. 4.9a and the NPs in Fig. 4.9b.

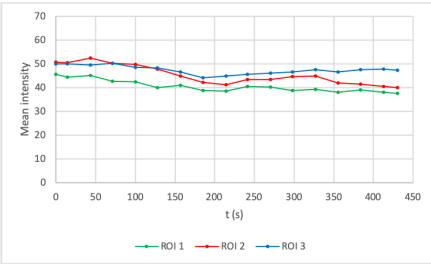

(a) Mean intensity of dextrans over the time of experiment measured in three ROIs.

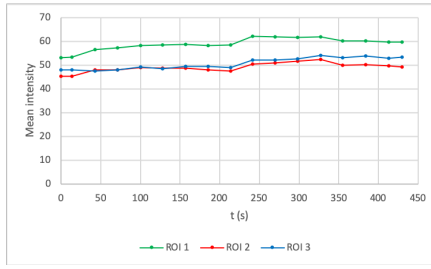

(b) Mean intensity of NPs over the time of experiment measured in three ROIs.

Figure 4.9: Mean intensities of dextrans and NPs over time in the ROIs shown in Fig. 4.8. (a) shows how the intensity of dextrans is quite constant, and (b) shows the same for the NPs. Lines with the same colour represent results obtained from the same ROI in the stack of images.

Accumulation of nanoparticles along the walls of the blood vessels

Two CAMs experienced accumulation of NPs along the inner walls of the blood vessels, and the recording from one of them is presented in the attached Video 2.
Figure 4.10 shows the phenomenon in this CAM. (a) is before injection of NPMBs and US exposure, while (b) shows how the NPs have lined the insides of parts of the vasculature after 6 min of insonation. From looking at the series of images, it seemed like the NPs were still contained inside the vessels and had not extravasated. The NP lining was quite homogeneous, and seemed to favour the small vessels as opposed to the bigger one they branch from. The FOV is the same as presented in Section 4.2.4, where vasoconstriction has been analyzed. The initial diameters of the vessels where found there and the ROIs are shown in Fig. 4.17. The blood vessel in the upper half of the images had a diameter of 176 μm before US exposure, while the one it branches from was initially 350 μm wide.

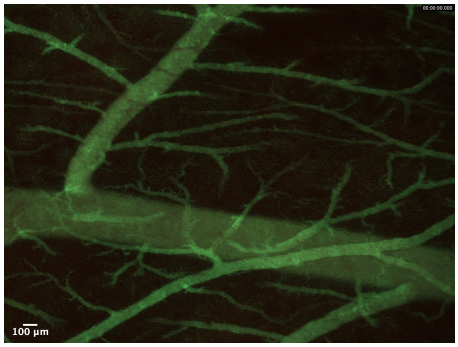

(a) The blood vessels before injection of NPMBs and US exposure.

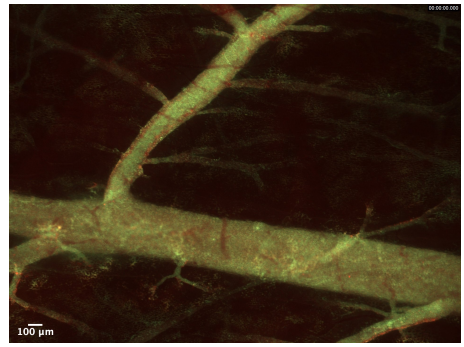

(b) The blood vessels after 6 min of US treatment, showing how the NPs have accumulated along the walls.

Figure 4.10: NP accumulation along the walls of insonated blood vessels. (a) is before NPMB injection and US treatment, (b) is after 6 min of US exposure. Post-US, the NPs have aggregated along the inside of the vessel walls, especially in the narrower blood vessels.

Accumulation of nanoparticles in small blood vessels

The feature of NP aggregates seemingly favouring accumulation in the lower range of vessel width was seen in half of the successful experiments. As with most of the other accumulation patters, it was exclusively seen in US-treated vasculatures. In the CAM shown in Fig. 4.11 the NPs have accumulated in vessels with diameters of 20-100 µm. The large one traversing the FOV is about 500 µm wide and do not portray the same property. The image was taken 41 s into the US treatment.

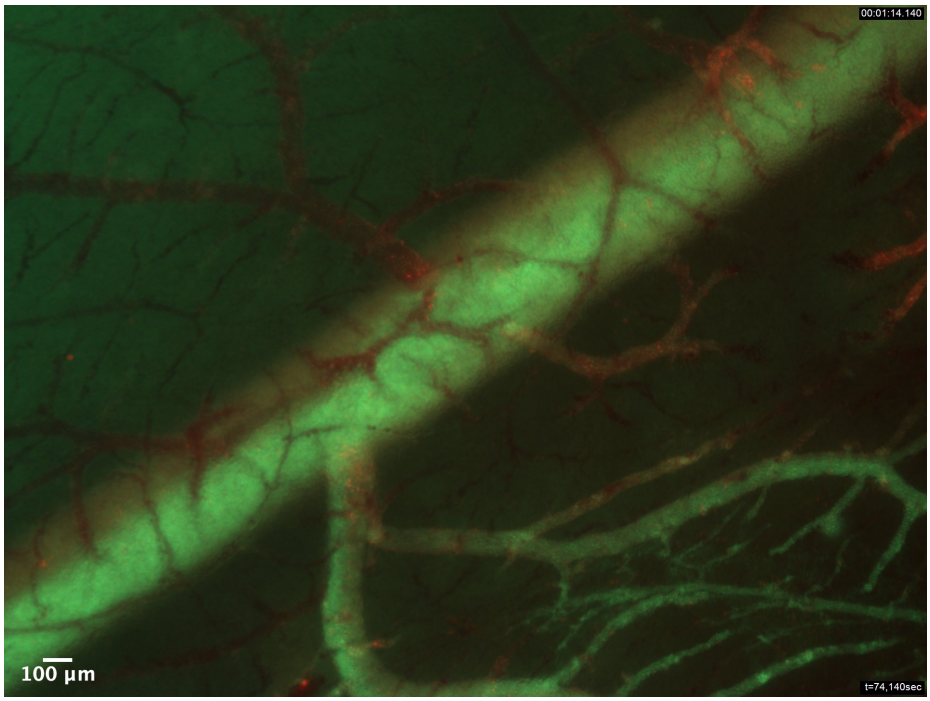

Figure 4.11: A CAM showing the phenomenon of NP accumulation located mainly to small vessels. The vessels accumulating NPs have diameters of 20-100 µm, while the large one they branch from is about 500 µm across. The image was taken 41 s into the process of US exposure.

Accumulation of nanoparticles at site of hindered perfusion

One experiment showcased a quite extreme degree of NP accumulation that was presumably caused by hindered perfusion. The recorded series of images are shown in the attached Video 3. A selection of the images is also showcased in Fig. 4.12. The front of dextrans seen in the middle of the FOV was close to a standstill through the whole duration of imaging, only moving slightly back and forth at the pulse of the embryo. The FOV shown was the second site imaged for this CAM, and the duration from catheterization to imaging is estimated to be around one hour. It is reasonable to assume that both the blood volume and pulse of the culture were drastically reduced by this time, resulting in a low blood perfusion rate.

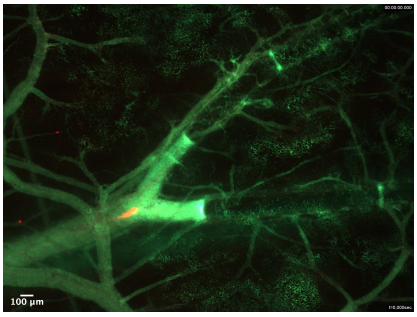

(a) Before insonation, t = 0.

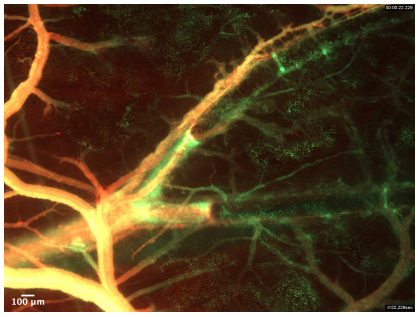

(b) NPMB entry, t = 22 s. The insonation has not been started yet.

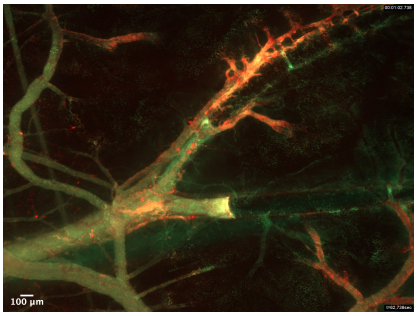

(c) During insonation, t = 279 s.

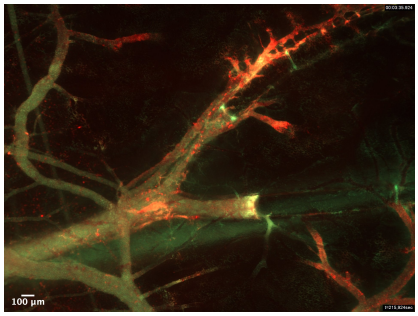

(d) After insonation, t = 432 s.

Figure 4.12: Hindered perfusion in one CAM lead to quite extreme accumulation of NPs. These figures show the front of dextrans in the middle of the frame that is almost at the same location through the entire duration of imaging. US treatment is started at t = 31 s. (a) shows the vasculature before insonation starts, and (b) presents the entry of NPMBs. (c) shows the initial NP accumulation during US exposure and (d) is after the US treatment is ended.

The mean intensity of the whole FOV was measured in a stack of 20 images from the series of images taken. Figure 4.13 shows the results from this analysis, where the green line represents the dextrans and the red one represents the NPs. Spikes in the signals are seen at t = 22 s, caused by the NPMBs entering the FOV. After about 30 s it stabilizes and remains approximately the same during insonation.

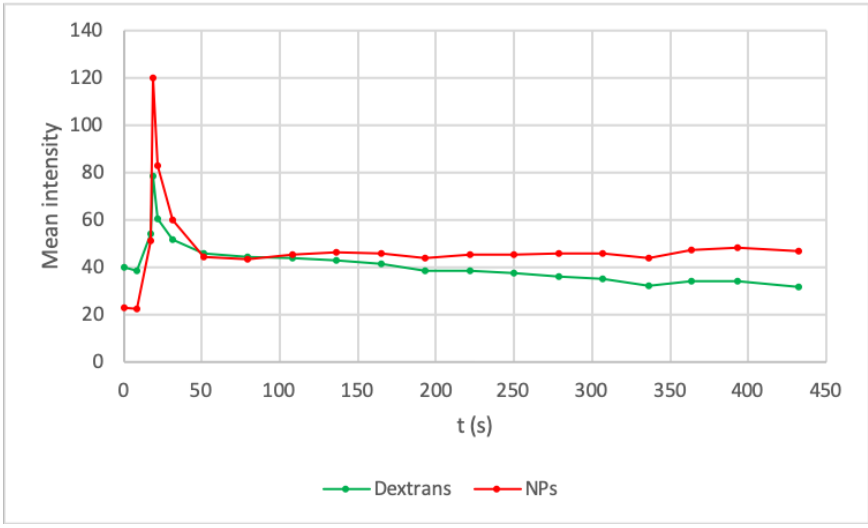

Figure 4.13: The mean intensities as a function of time of dextrans (green line) and NPs (red line) of the whole FOV in Fig. 4.12. NPMBs were injected at t = 22 s, and insonation started at t = 31 s.

The CAM was imaged 5, 10, 15, 20, 25 and 30 min after US treatment was ended, and the images are shown in Fig. 4.14. (a)-(f) show the extensive, gradual accumulation of NPs in the vessels. The front of dextrans initially seen in the middle of Fig. 4.12a is very slowly pushed further and further upwards.

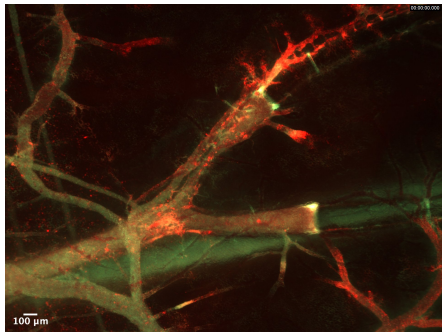

(a) 5 min after US treatment.

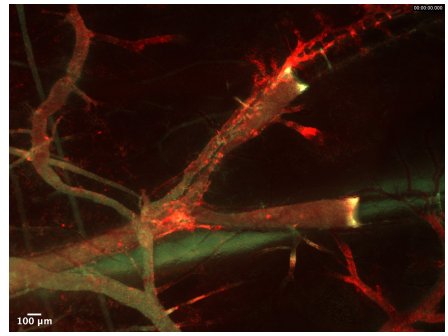

(b) 10 min after US treatment.

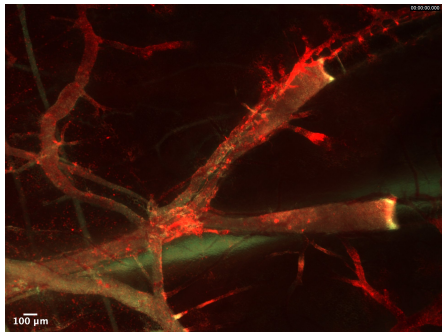

(c) 15 min after US treatment.

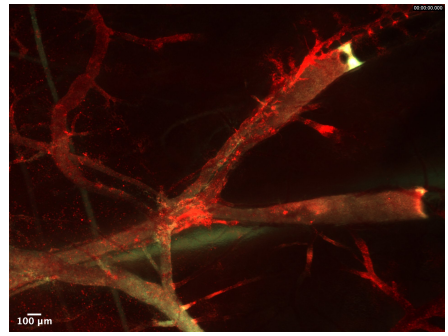

(d) 20 min after US treatment.

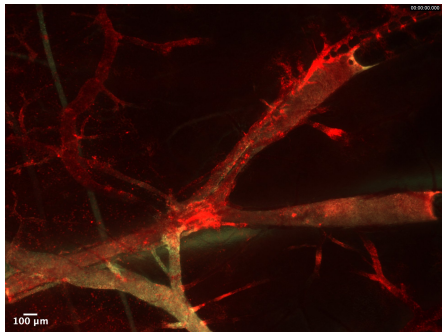

(e) 25 min after US treatment.

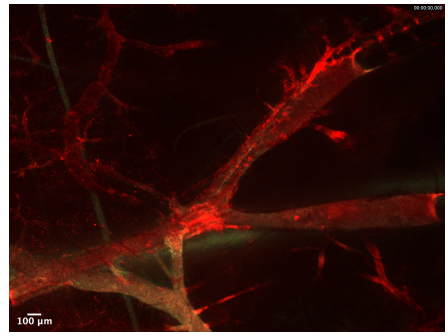

(f) 30 min after US treatment.

Figure 4.14: The vessels in the FOV from Fig. 4.12 was imaged 5, 10, 15, 20, 25 and 30 min after insonation was ended. (a)-(f) show how NPs continue to accumulate in the vasculature, with time after ended US treatment given below.

The six post-images were added to the image stack for Fiji analysis and the mean intensities through the entire experiment are graphed in Fig. 4.15. The green line represents the dextrans, and shows how the intensity gradually decreases after the spike. The decrease is likely caused by the fact that the dextrans loose fluorescence quite rapidly with time. The intensity of the NPs in red is more stable after the spike, but is slowly starting to fade after 15 min post-US.

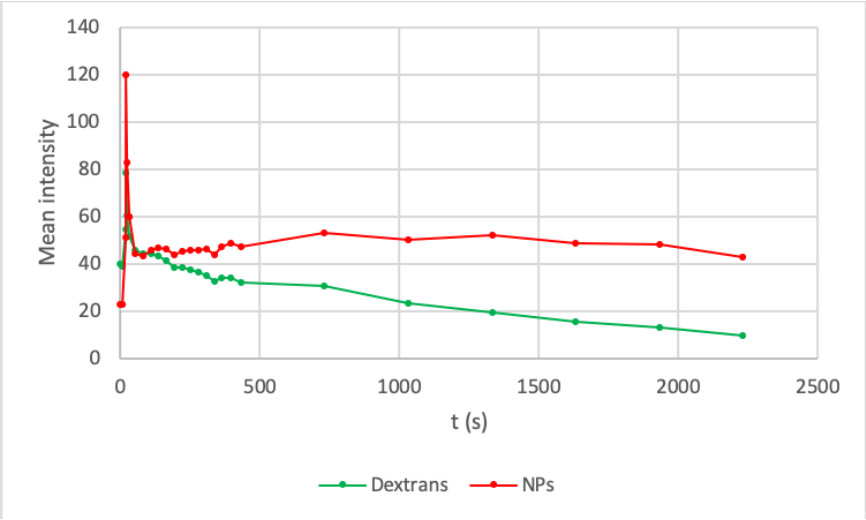

Figure 4.15: Mean intensities of dextrans (green line) and NPs (red line) in insonated vasculature where hindered perfusion presumably lead to a high level of NP accumulation. The NPMBs were injected at t = 22 s, and insonation started at t = 31 s.

4.2.4 Vasoconstriction

Ten of the imaged CAMs showed vasoconstriction during the process of US treatment.

The large vessel in the experiment shown in Fig. 4.2 was analyzed and revealed an average decrease in diameter of 30 %. The rate of vasoconstriction seems to be quite constant the first minutes of insonation, but towards the end it levels out. For this CAM, US exposure was initiated at t = 17 s.

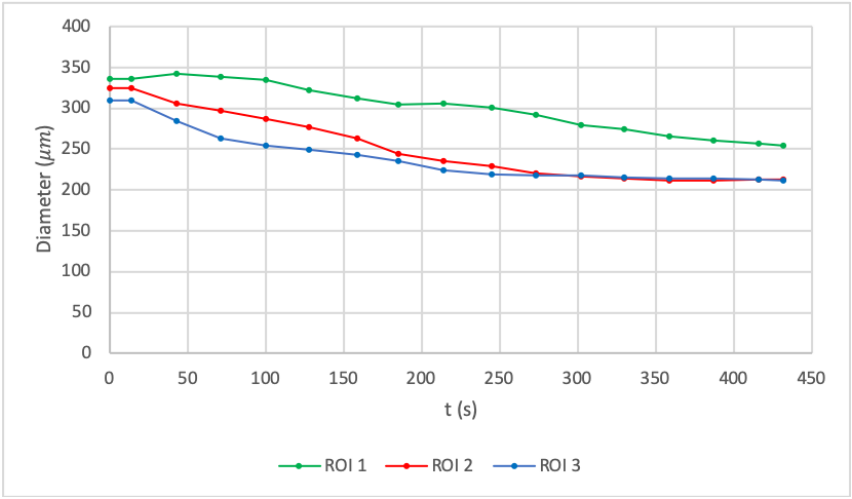

Figure 4.16: Decreasing vessel diameters in insonated vasculature over the time of experiment. ROI 1, 2 and 3 were measured perpendicular to the circular ROIs 1, 2 and 3 in Fig. 4.3.

Vasodilation followed by vasoconstriction

One CAM presented vasodilation prior to the vessels being constricted, and it is shown in the attached Video 2 and in Fig. 4.10. The subfigures (a) and (b) display how the vasculature looked before and after 6 min of US treatment. Two of the vessels were analyzed in Fiji, and the ROIs are shown in Fig. 4.17. ROI 1 and ROI 2 had initial diameters of 176 µm and 350 µm, respectively.

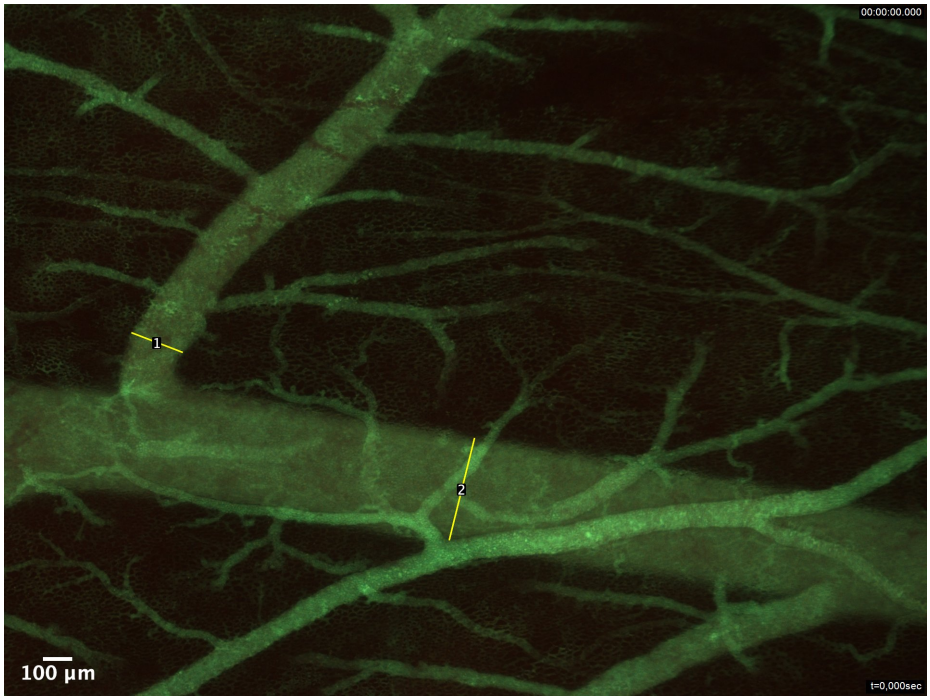

Figure 4.17: The ROIs used to analyze the vessels which experienced vasodilation followed by vasoconstriction. The diameters of ROI 1 and 2 were 176 µm and 350 µm, respectively, before US exposure.

The results from the analysis are shown in Fig. 4.18, where the diameters of ROI 1 and ROI 2 in Fig. 4.17 are averaged over the channels for dextrans and NPs. The blood vessel at ROI 1 had a total decrease of 18 %, by first dilating 19 % and then constricting 31 % from its peak diameter. The peak diameter of 209 µm was reached at t = 43 s. The blood vessel at ROI 2, on the other hand showed a total increase of 4 %. It first dilated by 15 % and then constricted 10 % from its peak diameter. The peak diameter of 403 µm was reached at t = 71 s.

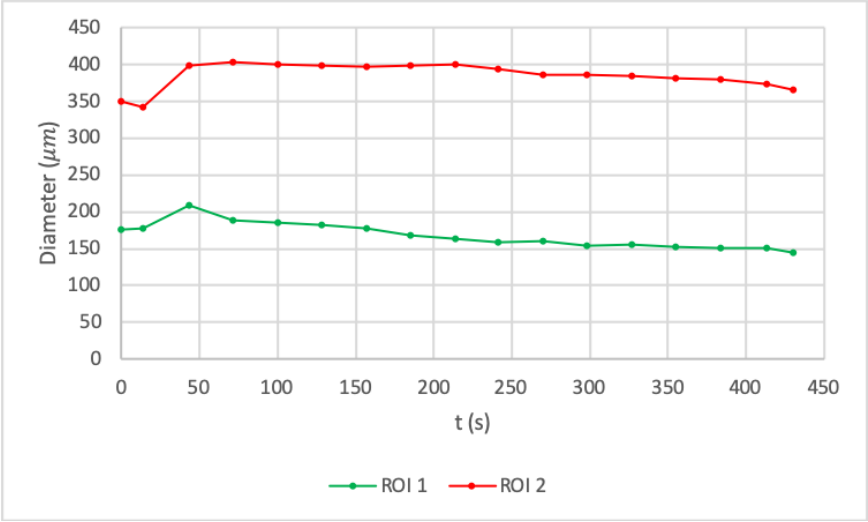

Figure 4.18: Mean diameter as a function of time for the ROIs presented in Fig. 4.17. Vasodilation followed by vasoconstriction was seen in this CAM, and the vasculature pre- and post-US is shown in Fig. 4.10. The green line shows the mean diameter of ROI 1 over time, and this vessel constricted a total of 18 %. The red line shows the mean diameter of ROI 2 over time, a vessel in which the diameter increased a total of 4 %.

4.2.5 Changes in perfusion

Visual inspection of individual particles of dextrans showed that the direction of perfusion switched back and forth quite frequently in numerous CAMs. For some it was rather rhythmical, resembling a breathing frequency, while others showed a higher degree of randomness. Switching of flow direction was seen in vasculatures both with and without US exposure. As it was challenging to illustrate the phenomenon with the recordings obtained for this thesis, an example from the specialization project is shown in Fig. 4.19. [47] Here, it was possible to showcase a tracked aggregate of NPs, shown by an arrow. A selection of images from the series is shown, together with its corresponding time after imaging was started. The attached Video 4, introduced in Section 4.2.3, shows an example of the phenomenon in a CAM experiment performed in the work for this thesis. Repeated switching of perfusion direction is seen in vessel at the top right, close to the ROIs 1 and 3 in Fig. 4.8.

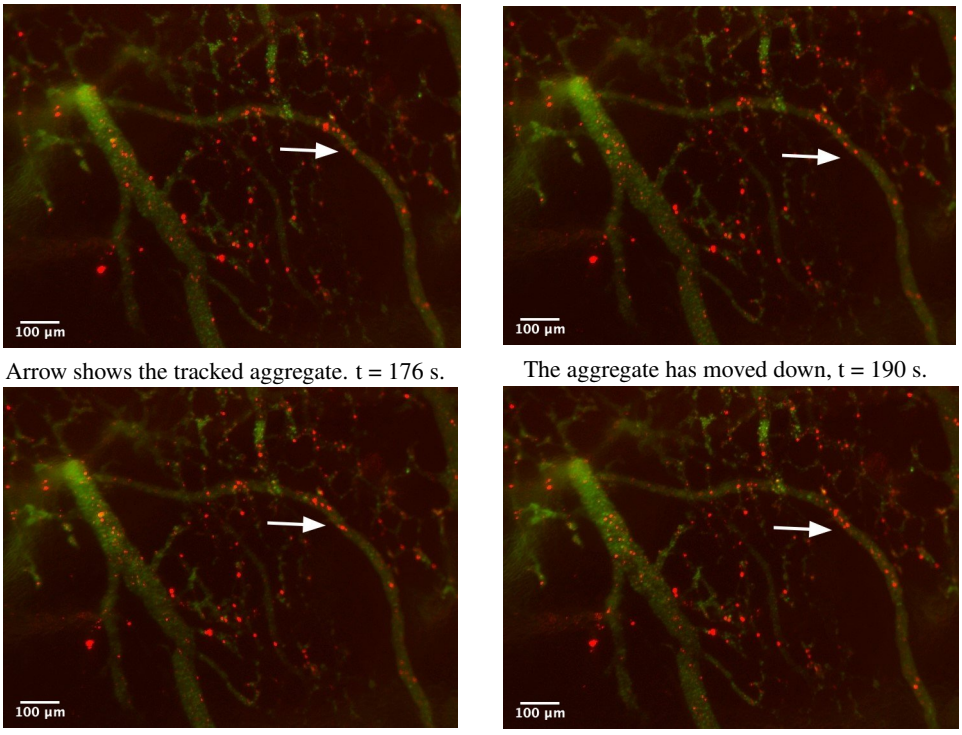

Arrow shows the tracked aggregate. t = 176 s.

The aggregate has moved down, t = 190 s.

The aggregate has moved up, t = 204 s.

The aggregate has moved down, t = 225 s.

Figure 4.19: A CAM from the specialization project showing the switching of blood flow direction. Four positions of the NP aggregate during the insonation are shown, together with the corresponding time after imaging was started. The arrow shows the aggregate of NPs that was tracked. The FOV was imaged in tumourous vasculature, and insonation was started at t = 1 s. The figure is retrieved from the specialization project report. [47]

4.2.6 Observations of leaky blood vessels and dark spots prior to US treatment

One of the CAMs revealed two phenomena only seen once in this study, and is presented in the attached Video 5. The vasculature seemed to be extra leaky already straight after injecting the dextrans. Additionally, dark spots were located close to some of the vessels. Figure 4.20 shows how the imaged FOV looked without NPMBs and pre-US. The dextrans had already leaked out and three dark spots are shown by arrows. From left to right, their diameters are 67, 32 and 71 µm, measured at their widest.

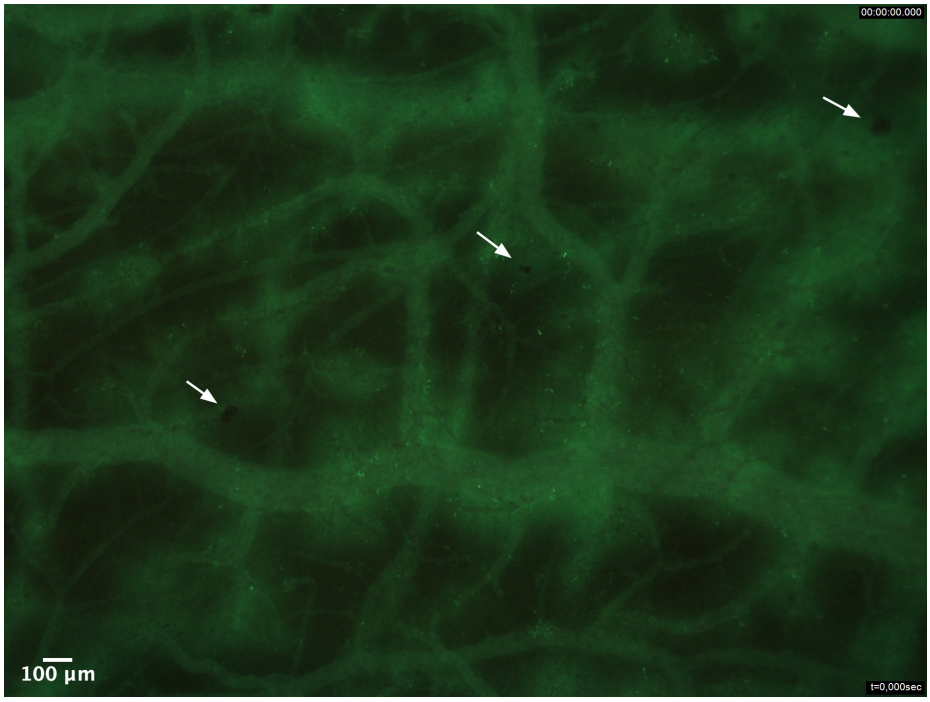

Figure 4.20: Leaky blood vessels prior to US treatment, with dark spots along them. Arrows point to the most visible ones. These two phenomena were only found in this one CAM.

After administration of NPMBs and 3.5 min of US treatment the FOV looked as shown in Fig. 4.21. It presents the pattern of NP accumulation shown in Section 4.2.3, a veil of NPs covering the vasculature. Clearly, more dextrans have extravasated from the vessels into the ECM.

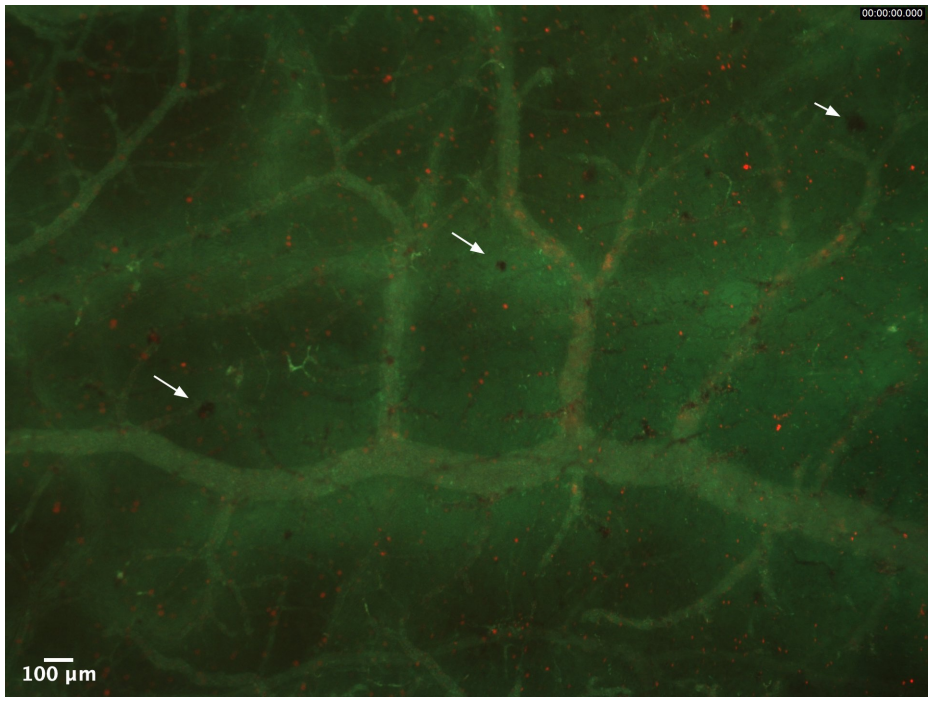

Figure 4.21: The leaky blood vessels after injection of NPMBs and US treatment. The NPs have accumulated as an overlaying veil, and more dextrans have extravasated out from the vessels. The dark spots are still visible and at the same locations as pre-US.

5 Discussion

5.1 The *ex ovo* cultures

Immense amounts of work have been put into making the CAM model perform as desired for the sake of studying drug delivery to tumours by sonopermeation. Also in our group, engineers and students have been working on improving the method for years and now it seems to function purposely. Nevertheless, there will always be challenges to conquer and improvements to make to obtain results of satisfactory quality. A lot of practice is required to master the techniques used in the method. In particular, cracking eggs, placing the catheter, and injecting dextrans and bubbles call for a steady hand and repeated training. With continued practice, the current success rate of 68 % may go up for future experiments. Normal development is not optimal without the protection and functions of the egg shell, and this is also a part of the reason for the low rate of embryo survival.

5.2 Ultrasound experiments with nanoparticle-stabilized microbubbles

The idea of improving the method by exchanging co-injection of dextrans and NPMBs with serial injections in a catheter was adopted by Stieger et al. [37] The modification had both its advantages and drawbacks in terms of the results obtained. The greatest advantage was the gained possibility of imaging the NPMBs as they entered the FOV, to be able to study their behaviour through the whole process of sonication and imaging. As presented in Section 3.4.1, they have a short circulation lifetime and so it was also beneficial to have the maximum amount of NPMBs present during imaging.

The most distinguished disadvantage attained was the increased level of difficulty the catheter introduced. Both placing it and making sure it remained in place during the injections was a great challenge. This gave fewer results than likely could have been achieved with co-injection, but on the other hand the data obtained was of higher quality and provided more information. For placing the catheter, small cannulas and sufficient lighting is advised.

To increase the fraction of CAMs possible to image inside a ring containing tumour cells, a sufficient number of inoculated sites is preferable. The number of rings per CAM culture was increased during this work, and inoculating 3 different sites was found to be

a satisfactory compromise. It was both practically possible, considering the limited space on the early CAM, and ultimately gave more data obtained in tumourous vasculatures.

5.2.1 Phenomena found by epi-fluorescent imaging during insonation

An important thing to keep in mind while studying the results presented in this thesis is the limited amount of data obtained. As seen from Table 4.1, just 18 different FOVs could be imaged and only two experiments with NPMBs were performed without US exposure. Naturally, this has a strong impact on the results in Table 4.2. In addition, the few control experiments done are not sufficient to conclude anything yet, but they suggest that without NPMBs and/or US no effects are produced in the CAM model.

The results just presented implies that US does indeed induce effects in the platform for drug delivery investigated. This is proposed based on the findings that most of the phenomena arose when the vasculature was exposed to US treatment. There are a few exceptions, but these are mainly related to the structure and properties of the vasculature itself.

The most relevant phenomena are discussed in greater detail in the following sections. The four latter in Table 4.2 are not included, as these were found less relevant for the scope of this thesis.

5.2.2 Extravasation of dextrans and nanoparticles

In relation to increasing drug delivery to tumours, extravasation is among the most important features to understand and control. Many have stated a positive correlation between extravasation and MI, but according to Stieger et al. this cannot be done uncritically. [37] The publication is summarized in Section 2.8. They found that the MI did not predict the frequency dependence of vascular effects as a function of frequency. In their study, the corresponding MI for the threshold pressure for extravasation was higher for the 2.25 MHz transducer compared to the 1.00 MHz transducer, 1.06 and 0.5, respectively. Their conclusion on this matter was that increasing the transmission pressure and decreasing the center frequency increased the rate and volume of extravasated material, but not without bound. They observed extravasation of fluid after low-stress insonation more frequently in capillary-sized vessels, with a small amount of dextran extravasation at each site. They suggest that for a drug delivery strategy, producing a widespread effect in capillaries by using low-stress parameters may result in a lower but more consistent concentration of extravasated drugs.

However, many other groups have found a positive correlation between MI and degree of extravasation. In a study aiming at delivering therapeutic agents to the brain, Cho et al. [48] found that disruption of the blood-brain barrier (BBB) in rats could be achieved with US and a circulating MB contrast agent, and that the results were MI dependent. They performed experiments to investigate the effects of different acoustic pressures on BBB disruptions and of blood vessels of various sizes, with the goal of determining vessel caliber dependence of the leakage and characterize the kinetics of the process. Based on time-dependent intensity change in the extravascular area, the leakages were classified into three types: fast, sustained, and slow. Fast leakage was characterized by a rapid increase to peak intensity during US exposure, and followed by a decrease. Sustained leakage was

indicated by a similar, immediate increase to peak intensity but remained elevated for the duration of imaging, occurring at low-to-intermediate pressures. Slow leakage began 5-15 min after US treatment, dominating at low pressures. This kind was more prevalent among smaller vessels than fast and sustained leakage. Fast leakage occurred at all pressures and vessel sizes. The conclusion was that it is possible to control leakage type and vessel size in US-induced BBB opening through varying the applied acoustic pressure. The observations of slow extravasation presented in Section 4.2.2 are comparable to the slow leakage seen in their study. The onset of extravasation was much faster, at initiation of US exposure instead of after 5-15 min, but the steady rate of extravasation is similar. The burst extravasations also presented in the same section of this thesis are to a certain extent equivalent to the fast leakages from the brain endothelial cells (ECs).

Also some of our collaborators using the same NPMBs as in this study have found a dependence between extravasation and tumour uptake of NPs, and the MI applied. [49] They investigated US-enhanced drug delivery in prostate cancer xenografts in athymic mice, where the tumours were exposed to US treatment of MI 0.15 and 0.4. The amount of NPs taken up by the tumour cells were found to increase by elevating the acoustic pressure, confirmed both in the periphery and in the central regions of the tumour. The authors propose three mechanisms that may be important in the process. One is the detachment of NPs because of US-induced MB destruction, resulting in a locally very high concentration of NPs in the vessels exposed to FUS. These free NPs, in addition to the ones already present in the solution, could extravasate simply due to the EPR effect. This hypothesis is supported by others, as the delivery of NPs was improved when the NPs were physically linked to MBs compared to a co-injected solution of the two. [50] Second, inertial cavitation causing violent MB collapses and jet streams could generate pores in the vessel walls. [51; 52] A wide range of articles state that pore formation is a crucial part of extravasation. Among them, Kooiman et al. [19] reported that the degree of pore formation is likely to correlate with MB behavior. Stable cavitation seems to induce small pores, while larger pores are probably due to the inertial cavitation of MBs. The extravasation could be hindered by the rapid resealing of the blood vessels, the time span ranging from a few milliseconds to several seconds. [19; 29] The result would be closing of the pores, which could lead to less extravasation of freed NPs. Thirdly, the effects resulting from inertial cavitation can affect the released NPs so that they are pushed across the capillary wall and into the ECM of the tumour.

Targeted MBs have been found to sonoporate ECs *in vivo*. [53] Sonoporation was studied by intravital microscopy using the model drug propidium iodide (PI). PI and MBs targeted to $\alpha_v\beta_3$-integrin were injected into CAMs and insonated. EC PI uptake was observed in 48 % of MB-vessel-wall complexes at 150 kPa (n = 140) and in 33 % at 200 kPa (n = 140). Efficiency of PI uptake depended on the local targeted MB concentration and increased up to 80 % for clusters of 10-16 targeted MBs. US or targeted MBs alone did not induce PI uptake, extravasation of red blood cells (RBCs) or vessel rupture was not noticed at the low acoustic pressures applied.

Burst extravasation

The burst extravasation from vessels exposed to US treatment can be seen in relation to the mean fluid velocities presented in Stieger et al. [37] The fact that they found higher velocities for higher acoustic pressures is likely caused by greater forces acting on the walls of the blood vessels. Therefore, it is also reasonable that it could cause an increased number of vessel ruptures. Additionally, they predicted different motions for the extravasated fluid from larger vascular openings for the high-stress class compared to smaller ruptures of the low-stress class. With a vascular gap diameter of 0.5 μm, the extravasated fluid was assumed to travel spherically, while for the 1 μm ruptures it was anticipated to travel conically. The latter was expected because for larger openings, the peak velocity oriented perpendicular to the vessel axis is greater.

A comparable study to this work was done by Davies et al. [54], but is not published yet. It is in the process of being accepted in "Ultrasound in Medicine Biology". They studied the effects of NPMBs and FUS on tumours growing in dorsal skinfold window chambers in mice. They subjected the FOVs to MIs of 0.2, 0.4, 0.6 or 0.8, and found that the rate and extent of penetration into the ECM increased with increasing MI. Contrastingly to what was seen in this work, the smaller blood vessels required higher MIs (0.8) to experience extravasation, than vessels with larger diameters. Such a high MI was not tested in the experiments for this thesis, but would absolutely be an appealing area of focus for future work. Possibly is could lead to controllable, slow extravasation from smaller vessels, and not only burst extravasations as seen when subjected an MI of 0.4.

However, an overlapping observation done by Davies et al. [54] was that they also discovered extravasation occurring at or close to vessel branching points. They claim that part of the reason could be the chaotic tumour vasculature, presenting trifurcations and branches of uneven diameters. This render the branching points more fragile, making them more susceptible to US treatment. [55; 56] It was also reported that microdisruption occurred more often at branching points, which could be due to MBs being more easily trapped at such locations. [57]

Movement of extravasated material into the ECM

The distance in which the extravasated material traveled into the tissue was also studied by Davies et al. [54] The results are not a complete match of the ones found in the CAM model. For MI 0.4, the maximum penetration of dextrans into the skin tissue was in the range of 34-77 μm, while the NPs penetrated in the range of 16-77 μm away from the vessel. The size difference between the dextrans and the NPs are proposed as the most probably reason for this discrepancy. The diameter of the NPs is approximately 160 nm, while the diameter of the 2 MDa dextrans is reported to be about 60 nm. [58] The dextrans and NPs penetrated the same distance in the CAM, approximately 300 μm, as seen from Fig. 4.5. The disparity between the results in skin tissue and the CAM could be explained by their differences in density. The gel-like CAM is a lot less dense than the skin tissue in the dorsal windows, probably making it easier to penetrate through.

It should be emphasized that the estimates of penetration distances is semi-quantitative, as it is currently not possible to confirm from which blood vessels the dextrans and NPs originate. The CAM is a 3D structure and the particles may have extravasated from vessels

above or below the image plane.

5.2.3 Accumulation of nanoparticles

Apparent veil of nanoparticles on top of the vasculature

The overlaying veil of NPs seen for several CAMs was also found by Salomonsen [59] in her master's thesis, while performing practically the same experiments as described in this thesis. The results are quite surprising, as one would rather expect the NPs to be flowing inside distinct vessels as opposed to being randomly distributed. The veil appears to stay more or less at the same location during imaging, and the gradual accumulation of NPs is prevalent. The sites that already had NPs located to them grew bigger and brighter, indicating accumulation of more particles. New sites of NP accumulation also arose, and the same gradual build-up was seen there. It is suspected that the veil might not be an actual effect, but merely that NPs from different imaging planes are visible at the same time.

Accumulation of only a few aggregates of nanoparticles

The cause for the apparently low presence of NPs in some CAMs is not yet known. As already mentioned in Section 4.2.3, there could be something wrong with the particular batch of NPMBs used. This hypothesis seems likely since the data presented the same results in all three successful injections and was not seen again for other NPMB batches.

However, because the suspicions of a faulty NPMB batch were declined by the producer at SINTEF, it was suspected that a different set of image settings could have been used by a mistake. The microscope settings were double checked for all the experiments in question, but no aberrations were found from the rest of the data set.

Other deviations in the execution of the experiments could have happened, leading to these irregular results. The most probable reason could be that inadequate injections of NPMBs were classified as successful, giving false positives. However, in that case no NPs at all would have been visible in the microscope and it also seems unlikely that it should have occurred in 3/3 experiments for this batch.

A possible explanation was stated by Davies et al. [54] in a study where they used the very same US transducer and type of NPMBs as in this work. They postulate that the NPMBs could have been destroyed by the applied acoustic power before reaching the FOV, since the size of the FUS beam is considerably larger than the FOV. Thus, new NPMBs would not be able to enter the FOV in time to replace the ones destroyed. However, the possibility of this hypothesis being applicable in this case is rather low as the phenomenon only appeared in one out of eight rounds of experiments.

Accumulation of nanoparticles along the walls of the blood vessels

From the series of images obtained in this study, it seems like the NPs have not been able to pass through the endothelium. At least for solid tumours the ability of NPs to penetrate far into the ECM is normally poor [60], but the results shown in Section 4.2.2 and discussed in Section 5.2.2 suggest that extravasation is possible in the more viscous CAM model.

The NP lining of the vessels was only seen in insonated CAMs in this work, and acoustic radiation forces has been suggested to contribute to the phenomenon in previous studies. [61] The steady flow of acoustic streaming can produce a translational force that pushes the particles against the blood vessel walls. In a solid tumour, this can also result in a longer retention time and increased accumulation. [62] Possibly, this can in some degree be extrapolated to normal vasculature in the CAM model.

Another possible explanation could be that the NPs are somewhat adhesive and tend to attach to the endothelium of the blood vessels. This has been occasionally observed for these SINTEF NPs by other researches in our group, but is not documented anywhere yet.

As with many concepts, a combination of contributions seems likely. In terms of drug delivery, an ideal solution could contain the following factors: 1) Acoustic radiation forces would push the NPs towards the walls of the blood vessels. 2) The effect of these forces could be enhanced by the forces of vasoconstriction working in the opposite direction. The combination would be a greater net force pushing the NPs outwards. 3) The NPs would have a high affinity for the endothelium inside the vessels, but once through they would favour traveling far into the ECM and reach the tumour cells.

Accumulation of nanoparticles in small blood vessels

One can imagine that the NP stickiness and acoustic streaming just discussed can also assist in the accumulation of NPs in small vessels. Logically, a narrow passage would get clogged faster than a wider one, leading to an easier build-up of NP aggregates.

The work by Bertuglia [63] presented in Section 5.2.4 showed persistence of MBs in terminal arterioles, capillaries, and small venules in reperfusion. Comparing the findings to other similar studies [64; 65; 66] , it is argued that MBs reflect the US waves mainly within the capillaries without disrupting the local environment. Most MBs were found to be entrapped in small arterioles, while only some larger arterioles had MB aggregates that periodically became dislodged and moved downstream.

Accumulation of nanoparticles at site of hindered perfusion

The reason for the hindered perfusion in the particular blood vessels that gave elevated NP accumulation is likely to be caused by a very slow blood perfusion. The site of imaging was the second one for this CAM, and the time span from catheterization to the second round of US exposure and imaging is estimated to be around one hour. By this time the chicken embryo could already be close to dead, resulting in a very weak pulse. However, for the other CAMs imaged at multiple sites the same challenge was not met. This disparity could simply be explained by individual differences between the cultures. Anyhow, from a clinical point of view a non-moving perfusion is not realistic in patients, even though US sonication is reported to slow it down. [54] As discussed more in Section 5.2.5 the decrease in perfusion velocity was found to correlate with the MI applied.

Another possible contribution could be constricted vessels outside the FOV blocking the blood flow to the imaged area. [57] Since this culture had been insonated prior to the second experiment, it is likely that some vessels were already constricted and not able to facilitate a normal perfusion rate. Vasoconstriction is discussed in greater extent in the next section.

5.2.4 Vasoconstriction

Raymond et al. [57] also found vasoconstriction in most of their experiments of US- and MB-enhanced drug delivery in the brains of mice. They observed it in both primary vessels and branching efferents, and suggest that the phenomenon is related to the properties of the smooth muscle present. Still, many of the vessels did not constrict, including capillaries, probably because they lack smooth muscles necessary for vasomotor capability. [67] Venoconstriction was not seen either, which strengthens the hypothesis as these contain considerably less smooth muscle than arteries. Arteliolar vasoconstriction has also been seen in many other studies, among them in rabbits [68], in rat brains [48] and in mice [69]. In the latter, Goertz et al. found that US-stimulated MBs alone could induce vascular damage, shutdown blood flow, and thereby inhibit tumour growth. Such shot-downs have been linked to increases in necrosis and apoptosis. [70]

Vasodilation followed by vasoconstriction

The first study to demonstrate vasodilation in human arteries caused by low-frequency US was published by Iida et al. in 2006. [71] The potential vasodilator effects of non-invasive transcutaneous low-frequency US in human brachial arteries was evaluated. Additionally, it was the first article presenting data regarding the duration of the vasodilator effect after treatment with low-frequency US *in vivo*. Significant degrees of vasodilation after 2 min of US treatment compared with baseline values were found, and it lasted up to 20 min. At 5 min of insonation, the brachial artery diameter increased by 4.1 %. Furthermore, the arteries continued to dilate even after US exposure. At 3 min after US treatment there was a 5.4 % increase, and at 5 min after US exposure a 6.0 % increase in vessel diameter ($p < 0.001$). These diameters returned to baseline dimensions about 20 min after the US was turned off. The findings of vasodilation in this thesis correspond only in some ways to those found by Iida et al. The rapid onset of dilation is similar, but the initial dilation is more substantial. Most importantly, the dilation is quickly replaced by vasoconstriction as opposed to the continued dilation they saw. They state that although the mechanism of vasodilation induced by low-frequency US is not entirely known, it is likely to be due to a local vasodilator effect related to stimulation of ECs by local vibrations from the US. Vascular ECs normally respond with several mechanical stresses, including shear tension and compression. US is a propagating pressure wave that transfers mechanical energy to tissues, and Krasovitski and Kimmel have found that shear stress is induced at tissue walls in an US field. [72]

Vasodilation caused by combining MBs and US exposure has also been shown by Bertuglia in ischemia/reperfusion events as the vessels were exposed to an MI of 1.3. [63] Among their main results was that low-intensity US and MBs caused vasodilation in arterioles in the hamster cheek pouch microcirculation following postischemic reperfusion. When the MBs were injected without the presence of US exposure, they did not see any significant change in the diameter of the vessels. The same was confirmed in this work, as no signs of vessel constriction was found without US treatment.

The production of nitric oxide (NO) in the vessels has been suggested to engage in vasodilation, and the effects were found to increase by utilizing MBs and US. [63; 73]

5.2.5 Changes in blood perfusion

The most ubiquitous observation in the results was the repeating change in the direction of perfusion in the CAM vasculature. It was most commonly seen in insonated vessels, but it also occurred in experiments without US. Especially for insonated vessels the switching appeared rather rhythmical, often at the same pulse as the US. An interesting discovery found in the specialization project was that it seemed to be much more common in vessels treated with MI 0.4 rather than MI 0.8. Only one example of switching while exposed to an MI of 0.8 was identified then. [47] The mechanisms responsible for the phenomena are not fully understood, but a few suggestions are investigated.

Nonetheless, the phenomenon of perfusion switching is not new to our group. Petros Tesfamichael Yemane is currently studying drug delivery to tumours in skinfold dorsal windows in mice, and has confirmed the repeated switching of perfusion direction. [54] In the study, US treatment of the vessels proved to change the blood flow rate and direction of perfusion. The effects were found for all MIs tested (0.2, 0.4, 0.6, 0.8), but were more pronounced for the highest one. By tracking individual dextran particles, they managed to analyze the altered velocity of blood perfusion inside the vasculature. Prior to US treatment, after injection of NPMBs, the velocity was 117 ± 40 μm/s. After applying US, the velocity of NPs decreased by approximately 41 %, 63 %, and 89 % for MIs of 0.2, 0.4, and 0.8, respectively. Moreover, US combined with MBs altered the blood flow direction, and the percentage of occurrence increased with MI. For the highest MI, approximately 50 % of the recordings showed a change in the flow direction. No observations of change in flow direction was seen without the application of US. A reduction of blood velocity and perfusion due to US-induced MBs (MIs 0.74-1.6) were also supported by other studies. [69; 70; 74]

The MIs used by Tarapacki et al. [38], their work presented in Section 2.8, are comparable to the ones in this thesis. Naturally, the results are therefore of great interest when published in full. The settings that induced transient decreases in perfusion correspond to an MI of 0.34, while the permanent vascular damages occurred at MI 0.45.

Others that have studied US-induced changes in perfusion are Keravnou et al. [75] The effects of acoustic pressure (MIs 1.7-4) and number of cycles (20 or 1000 cycles) were examined. Perfusion changes caused by the action of US on MBs in the microcirculation were qualitatively and quantitatively assessed with contrast-enhanced US. Areas that were exposed to MI $>$ 1.7 MPa underwent a detectable and irreversible perfusion change. Complete devascularization of the US exposed area was observed at much larger acoustic pressures (MI $\sim$ 4). Shorter acoustic pulses (20 cycles) produced markedly fewer perfusion changes than longer pulses (1000 cycles) under the same acoustic amplitude exposure.

The change in blood flow has been associated with inertial cavitation, which is induced in the higher range of MIs. [76] However, the phenomenon was also found even at MIs as low as 0.2 where inertial cavitation can be ruled out, indicating that additional mechanisms are involved. Some of the mechanisms suggested by Goertz et al. are: 1) Aggregation and activation of platelets that apparently could occur very rapidly after an injury to the ECs due to rapid destruction of MBs at the surface of tumour vasculature, thereby reducing the blood flow. [56] 2) There might be a significant cavitation activity going on in nearby arterioles outside the FOV that potentially can induce vasoconstriction and affect the flow

within the FOV. The occurrence of vasoconstriction has been reported to induce a reduction and transiently stop blood flow. [57]

5.2.6 Observations of leaky blood vessels and dark spots prior to US treatment

Leaky blood vessels

The observation of the CAM possessing extra leaky blood vessel seemingly has a no more intricate explanation than the distinctive properties of this culture. Intravital imaging of vasculature and NPs have demonstrated large heterogeneity of the vascular permeability. [49; 77] Incomplete angiogenesis can be expected for tumourous vessels, but this CAM was imaged in what was assumed to be normal vasculature. However, since the ring of OHS cells is placed close to the embryo early in CAM development, it is possible that the cancer cells spread to healthy vessels as the ring is moved outwards together with the growing CAM. It is therefore possible that the vasculature in the FOV actually contains tumour cells, even though it was imaged outside the ring.

Dark spots prior to US treatment

Other studies have shown dark spots in their images of blood vessels and claim them to be RBCs. [48; 54] They are usually related to tissue damage caused by high acoustic pressures (MI ~ 0.8), but also to a decreased perfusion rate. The leakiness in these vessels has probably slowed down the flow rate enough to make the RBCs visible. Microhemorrhages have been found for an MI of 0.8, but no severe vascular damage was detected and no hemorrhages were seen for lower MIs. [48]

6 Implications and further work

Targeted drug delivery to tumours mediated by combining NPMBs and FUS continues to provide encouraging results, and the collection of effects studied in this thesis is no exception. The most important work ahead is acquiring a more complete data set to be able to confirm the features discussed in this thesis, and hopefully others too. Especially results that can establish whether the effects are caused by the acoustic pressure or not is crucial. Many other studies assign the degree of impact to the MI, presenting increased effects by elevating the acoustic power. Therefore, higher MIs with the current experimental set-up should be investigated. A variety of burst periods and frequencies could also be tested.

7 | Conclusion

This study has investigated the behaviour of NPMBs administered in vasculatures of chicken CAMs grown *ex ovo*. The blood vessels were insonated with an MI of 0.4, and imaged by real-time epi-fluorescent microscopy. Exposing the NPMBs to US was found to have a wide range of effects on both the NPMBs and the blood vessels. In one CAM the US seemingly increased the extravasation of dextrans and NPs into the ECM, which is a desired effect in terms of drug delivery to tumours. Other effects that were studied were various patterns of NP accumulation, vasoconstriction and -dilation, and changes in blood perfusion. Observations of the structure and properties of the CAM vasculatures were also presented, highlighting the numerous differences between individual cultures.

The final aim of this work is a more specific treatment of tumours, leading to less side effects and a shorter remission time for cancer patients. The combination of NPMBs and FUS as a platform for targeted drug delivery to tumours seems promising. However, the results in this thesis are only preliminary, and a lot of experimental and analytic work are yet to be done before favourable effects can be said to be confirmed.

Bibliography

[1] F. Bray, J. Ferlay, I. Soerjomataram, R. L. Siegel, L. A. Torre, and A. Jemal, "Global cancer statistics 2018: Globocan estimates of incidence and mortality worldwide for 36 cancers in 185 countries," *CA: a cancer journal for clinicians*, vol. 68, no. 6, pp. 394–424, 2018.

[2] World Health Organization, "Cancer fact sheet," September 2018.

[3] H.-P. Gerber, P. D. Senter, and I. S. Grewal, "Antibody drug-conjugates targeting the tumor vasculature: current and future developments," in *MAbs*, vol. 1, pp. 247–253, Taylor & Francis, 2009.

[4] S. Snipstad, "Boblende nanomedisin mot kreft," November 2016.

[5] R. A. Weinberg, "How cancer arises," *Scientific American*, vol. 275, no. 3, pp. 62–70, 1996.

[6] D. Hanahan and R. A. Weinberg, "The hallmarks of cancer," *cell*, vol. 100, no. 1, pp. 57–70, 2000.

[7] T. N. Seyfried and L. C. Huysentruyt, "On the origin of cancer metastasis," *Critical reviews in oncogenesis*, vol. 18, no. 1-2, p. 43, 2013.

[8] N. Nishida, H. Yano, T. Nishida, T. Kamura, and M. Kojiro, "Angiogenesis in cancer," *Vascular health and risk management*, vol. 2, no. 3, p. 213, 2006.

[9] D. W. Siemann, "The unique characteristics of tumor vasculature and preclinical evidence for its selective disruption by tumor-vascular disrupting agents," *Cancer treatment reviews*, vol. 37, no. 1, pp. 63–74, 2011.

[10] P. U. Atukorale, G. Covarrubias, L. Bauer, and E. Karathanasis, "Vascular targeting of nanoparticles for molecular imaging of diseased endothelium," *Advanced drug delivery reviews*, vol. 113, pp. 141–156, 2017.

[11] A. Schroeder, J. Kost, and Y. Barenholz, "Ultrasound, liposomes, and drug delivery: principles for using ultrasound to control the release of drugs from liposomes," *Chemistry and physics of lipids*, vol. 162, no. 1-2, pp. 1–16, 2009.

[12] A. Carovac, F. Smajlovic, and D. Junuzovic, "Application of ultrasound in medicine," *Acta Informatica Medica*, vol. 19, no. 3, p. 168, 2011.

[13] P. R. Hoskins, K. Martin, and A. Thrush, *Diagnostic ultrasound: physics and equipment*. Cambridge University Press, 2010.

[14] T. Şen, O. Tüfekçioğlu, and Y. Koza, "Mechanical index," *Anatolian journal of cardiology*, vol. 15, no. 4, p. 334, 2015.

[15] J. E. Aldrich, "Basic physics of ultrasound imaging," *Critical care medicine*, vol. 35, no. 5, pp. S131–S137, 2007.

[16] V. Chan and A. Perlas, "Basics of ultrasound imaging," in *Atlas of ultrasound-guided procedures in interventional pain management*, pp. 13–19, Springer, 2011.

[17] W. D. OâĂŹBrien Jr, "Ultrasound–biophysics mechanisms," *Progress in biophysics and molecular biology*, vol. 93, no. 1-3, pp. 212–255, 2007.

[18] F. Kiessling, S. Fokong, P. Koczera, W. Lederle, and T. Lammers, "Ultrasound microbubbles for molecular diagnosis, therapy, and theranostics," *Journal of nuclear medicine*, vol. 53, no. 3, p. 345, 2012.

[19] K. Kooiman, H. J. Vos, M. Versluis, and N. de Jong, "Acoustic behavior of microbubbles and implications for drug delivery," *Advanced drug delivery reviews*, vol. 72, pp. 28–48, 2014.

[20] P. C. Sontum, "Physicochemical characteristics of sonazoidâĎć, a new contrast agent for ultrasound imaging," *Ultrasound in medicine & biology*, vol. 34, no. 5, pp. 824–833, 2008.

[21] Ý. Mørch, R. Hansen, S. Berg, A. K. Åslund, W. R. Glomm, S. Eggen, R. Schmid, H. Johnsen, S. Kubowicz, S. Snipstad, *et al.*, "Nanoparticle-stabilized microbubbles for multimodal imaging and drug delivery," *Contrast media & molecular imaging*, vol. 10, no. 5, pp. 356–366, 2015.

[22] S. S. Rane and P. Choi, "Polydispersity index: how accurately does it measure the breadth of the molecular weight distribution?," *Chemistry of materials*, vol. 17, no. 4, pp. 926–926, 2005.

[23] V. S. Kulkarni, *Handbook of non-invasive drug delivery systems: science and technology*. Elsevier, 2009.

[24] S. Snipstad, "Cellular uptake of iron oxide nanoparticles and the effect of ultrasound," no. NTNU Specialization project, not published, 2012.

[25] B. Gupta, T. S. Levchenko, and V. P. Torchilin, "Intracellular delivery of large molecules and small particles by cell-penetrating proteins and peptides," *Advanced drug delivery reviews*, vol. 57, no. 4, pp. 637–651, 2005.

[26] A. M. Holban and A. M. Grumezescu, *Nanoarchitectonics for Smart Delivery and Drug Targeting*. William Andrew, 2016.

[27] D. K. Chatterjee, P. Diagaradjane, and S. Krishnan, "Nanoparticle-mediated hyperthermia in cancer therapy," *Therapeutic delivery*, vol. 2, no. 8, pp. 1001–1014, 2011.

[28] F. J. G. Prieur, "Ultrasound, cavitation, and cancer therapy."

[29] I. Lentacker, I. De Cock, R. Deckers, S. De Smedt, and C. Moonen, "Understanding ultrasound induced sonoporation: definitions and underlying mechanisms," *Advanced drug delivery reviews*, vol. 72, pp. 49–64, 2014.

[30] R. S. Meltzer, "Food and drug administration ultrasound device regulation: the output display standard, the âĂIJmechanical index,âĂİ and ultrasound safety," *Journal of the American Society of Echocardiography*, vol. 9, no. 2, pp. 216–220, 1996.

[31] I. Lentacker, S. C. De Smedt, and N. N. Sanders, "Drug loaded microbubble design for ultrasound triggered delivery," *Soft Matter*, vol. 5, no. 11, pp. 2161–2170, 2009.

[32] S. Snipstad, S. Berg, Ý. Mørch, A. Bjørkøy, E. Sulheim, R. Hansen, I. Grimstad, A. van Wamel, A. F. Maaland, S. H. Torp, *et al.*, "Ultrasound improves the delivery and therapeutic effect of nanoparticle-stabilized microbubbles in breast cancer xenografts," *Ultrasound in medicine & biology*, vol. 43, no. 11, pp. 2651–2669, 2017.

[33] S. Snipstad, E. Sulheim, C. de Lange Davies, C. Moonen, G. Storm, F. Kiessling, R. Schmid, and T. Lammers, "Sonopermeation to improve drug delivery to tumors: from fundamental understanding to clinical translation," *Expert opinion on drug delivery*, vol. 15, no. 12, pp. 1249–1261, 2018.

[34] Ø. Fodstad, A. Brøgger, Ø. Bruland, O. P. Solheim, J. M. Nesland, and A. Pihl, "Characteristics of a cell line established from a patient with multiple osteosarcoma, appearing 13 years after treatment for bilateral retinoblastoma," *International journal of cancer*, vol. 38, no. 1, pp. 33–40, 1986.

[35] O. M. Bellairs R., *Atlas of Chick Development 3rd Edition*. Academic Press, 2014.

[36] D. B. Murphy, *Fundamentals of light microscopy and electronic imaging*. John Wiley & Sons, 2002.

[37] S. M. Stieger, C. F. Caskey, R. H. Adamson, S. Qin, F.-R. E. Curry, E. R. Wisner, and K. W. Ferrara, "Enhancement of vascular permeability with low-frequency contrast-enhanced ultrasound in the chorioallantoic membrane model," *Radiology*, vol. 243, no. 1, pp. 112–121, 2007.

[38] C. Tarapacki, W. M. Kuebler, A. Tabuchi, and R. Karshafian, "Reversible and irreversible vascular bioeffects induced by ultrasound and microbubbles in chorioallantoic membrane model," in *AIP Conference Proceedings*, vol. 1821, p. 170002, AIP Publishing, 2017.

[39] A. S. Klymchenko, E. Roger, N. Anton, H. Anton, I. Shulov, J. Vermot, Y. Mely, and T. F. Vandamme, "Highly lipophilic fluorescent dyes in nano-emulsions: towards bright non-leaking nano-droplets," *RSC advances*, vol. 2, no. 31, pp. 11876–11886, 2012.

[40] A. K. Åslund, E. Sulheim, S. Snipstad, E. von Haartman, H. Baghirov, N. Starr, M. KvaÌŁle Løvmo, S. Lelú, D. Scurr, C. d. L. Davies, *et al.*, "Quantification and qualitative effects of different pegylations on poly (butyl cyanoacrylate) nanoparticles," *Molecular pharmaceutics*, vol. 14, no. 8, pp. 2560–2569, 2017.

[41] H. Baghirov, S. Melikishvili, Ý. Mørch, E. Sulheim, A. K. Åslund, T. Hianik, and C. de Lange Davies, "The effect of poly (ethylene glycol) coating and monomer type on poly (alkyl cyanoacrylate) nanoparticle interactions with lipid monolayers and cells," *Colloids and Surfaces B: Biointerfaces*, vol. 150, pp. 373–383, 2017.

[42] R. Müller, C. Lherm, J. Herbort, T. Blunk, and P. Couvreur, "Alkylcyanoacrylate drug carriers: I. physicochemical characterization of nanoparticles with different alkyl chain length," *International journal of pharmaceutics*, vol. 84, no. 1, pp. 1–11, 1992.

[43] E. Sulheim, H. Baghirov, E. Haartman, A. Bøe, A. K. Åslund, Ý. Mørch, and C. de Lange Davies, "Cellular uptake and intracellular degradation of poly (alkyl cyanoacrylate) nanoparticles," *Journal of nanobiotechnology*, vol. 14, no. 1, p. 1, 2016.

[44] Sigma-Aldrich, "Fluorescein isothiocyanate-dextran."

[45] The NC3Rs, "How much blood does a mouse have?."

[46] C. Kind, "The development of the circulating blood volume of the chick embryo," *Anatomy and embryology*, vol. 147, no. 2, pp. 127–132, 1975.

[47] K. Bråten, "Nanoparticle-microbubbles and focused ultrasound for targeted drug delivery to tumours - characterization in the chicken chorioallantoic membrane model," no. NTNU Specialization project, not published, 2019.

[48] E. E. Cho, J. Drazic, M. Ganguly, B. Stefanovic, and K. Hynynen, "Two-photon fluorescence microscopy study of cerebrovascular dynamics in ultrasound-induced blood-brain barrier opening," *Journal of Cerebral Blood Flow & Metabolism*, vol. 31, no. 9, pp. 1852–1862, 2011.

[49] S. Eggen, S.-M. Fagerland, Ý. Mørch, R. Hansen, K. Søvik, S. Berg, H. Furu, A. D. Bøhn, M. B. Lilledahl, A. Angelsen, *et al.*, "Ultrasound-enhanced drug delivery in prostate cancer xenografts by nanoparticles stabilizing microbubbles," *Journal of controlled release*, vol. 187, pp. 39–49, 2014.

[50] C. W. Burke, Y.-H. J. Hsiang, E. Alexander IV, A. L. Kilbanov, and R. J. Price, "Covalently linking poly (lactic-co-glycolic acid) nanoparticles to microbubbles before intravenous injection improves their ultrasound-targeted delivery to skeletal muscle," *Small*, vol. 7, no. 9, pp. 1227–1235, 2011.

[51] V. Frenkel, "Ultrasound mediated delivery of drugs and genes to solid tumors," *Advanced drug delivery reviews*, vol. 60, no. 10, pp. 1193–1208, 2008.

[52] H. Shankar and P. S. Pagel, "Potential adverse ultrasound-related biological effectsa critical review," *Anesthesiology: The Journal of the American Society of Anesthesiologists*, vol. 115, no. 5, pp. 1109–1124, 2011.

[53] I. Skachkov, Y. Luan, A. F. van der Steen, N. de Jong, and K. Kooiman, "Targeted microbubble mediated sonoporation of endothelial cells in vivo," *IEEE transactions on ultrasonics, ferroelectrics, and frequency control*, vol. 61, no. 10, pp. 1661–1667, 2014.

[54] C. de Lange Davies, P. Yemane, A. Åslund, S. Snipstad, A. Bjørkøy, K. Grendstad, S. Berg, Ý. Mørch, S. H. Torp, and R. Hansen, "Effect of ultrasound on the vasculature and extravasation of nanoscale particles imaged in real time," *Ultrasound in Medicine Biology*, no. To be accepted, 2019.

[55] D. Fukumura and R. K. Jain, "Tumor microenvironment abnormalities: causes, consequences, and strategies to normalize," *Journal of cellular biochemistry*, vol. 101, no. 4, pp. 937–949, 2007.

[56] X. Hu, A. Kheirolomoom, L. M. Mahakian, J. R. Beegle, D. E. Kruse, K. S. Lam, and K. W. Ferrara, "Insonation of targeted microbubbles produces regions of reduced blood flow within tumor vasculature," *Investigative radiology*, vol. 47, no. 7, p. 398, 2012.

[57] S. B. Raymond, J. Skoch, K. Hynynen, and B. J. Bacskai, "Multiphoton imaging of ultrasound/optison mediated cerebrovascular effects in vivo," *Journal of Cerebral Blood Flow & Metabolism*, vol. 27, no. 2, pp. 393–403, 2007.

[58] T. Lammers, P. Koczera, S. Fokong, F. Gremse, J. Ehling, M. Vogt, A. Pich, G. Storm, M. Van Zandvoort, and F. Kiessling, "Theranostic uspio-loaded microbubbles for mediating and monitoring blood-brain barrier permeation," *Advanced functional materials*, vol. 25, no. 1, pp. 36–43, 2015.

[59] M. L. Salomonsen, "Study of the chicken chorioallantoic membrane (cam) as an in vivo-model for ultrasound-mediated delivery of drugs using nanoparticle-stabilized- and standard ultrasound microbubbles," Master's thesis, NTNU, 2018.

[60] T. Lammers, F. Kiessling, W. E. Hennink, and G. Storm, "Drug targeting to tumors: principles, pitfalls and (pre-) clinical progress," *Journal of controlled release*, vol. 161, no. 2, pp. 175–187, 2012.

[61] T. Boissenot, A. Bordat, E. Fattal, and N. Tsapis, "Ultrasound-triggered drug delivery for cancer treatment using drug delivery systems: from theoretical considerations to practical applications," *Journal of Controlled Release*, vol. 241, pp. 144–163, 2016.

[62] P. A. Dayton, J. S. Allen, and K. W. Ferrara, "The magnitude of radiation force on ultrasound contrast agents," *The Journal of the Acoustical Society of America*, vol. 112, no. 5, pp. 2183–2192, 2002.

[63] S. Bertuglia, "Increase in capillary perfusion following low-intensity ultrasound and microbubbles during postischemic reperfusion," *Critical care medicine*, vol. 33, no. 9, pp. 2061–2067, 2005.

[64] S. B. Feinstein, "The powerful microbubble: from bench to bedside, from intravascular indicator to therapeutic delivery system, and beyond," *American Journal of physiology-heart and circulatory physiology*, vol. 287, no. 2, pp. H450–H457, 2004.

[65] J. R. Lindner, J. Song, J. Christiansen, A. L. Klibanov, F. Xu, and K. Ley, "Ultrasound assessment of inflammation and renal tissue injury with microbubbles targeted to p-selectin," *Circulation*, vol. 104, no. 17, pp. 2107–2112, 2001.

[66] D. M. Skyba, R. J. Price, A. Z. Linka, T. C. Skalak, and S. Kaul, "Direct in vivo visualization of intravascular destruction of microbubbles by ultrasound and its local effects on tissue," *Circulation*, vol. 98, no. 4, pp. 290–293, 1998.

[67] R. A. Hill, L. Tong, P. Yuan, S. Murikinati, S. Gupta, and J. Grutzendler, "Regional blood flow in the normal and ischemic brain is controlled by arteriolar smooth muscle cell contractility and not by capillary pericytes," *Neuron*, vol. 87, no. 1, pp. 95–110, 2015.

[68] K. Hynynen, A. H. Chung, V. Colucci, and F. A. Jolesz, "Potential adverse effects of high-intensity focused ultrasound exposure on blood vessels in vivo," *Ultrasound in medicine & biology*, vol. 22, no. 2, pp. 193–201, 1996.

[69] D. E. Goertz, M. Todorova, O. Mortazavi, V. Agache, B. Chen, R. Karshafian, and K. Hynynen, "Antitumor effects of combining docetaxel (taxotere) with the antivascular action of ultrasound stimulated microbubbles," *PloS one*, vol. 7, no. 12, p. e52307, 2012.

[70] K. BurkeCW *et al.*, "Inhibition of glioma growth by microbubble activation in a subcutaneous model using low duty cycleultra sound without significant heating," *JNeurosurg*, vol. 114, no. 6, pp. 1654–1661, 2011.

[71] K. Iida, H. Luo, K. Hagisawa, T. Akima, P. K. Shah, T. Z. Naqvi, and R. J. Siegel, "Noninvasive low-frequency ultrasound energy causes vasodilation in humans," *Journal of the American College of Cardiology*, vol. 48, no. 3, pp. 532–537, 2006.

[72] B. Krasovitski and E. Kimmel, "Shear stress induced by a gas bubble pulsating in an ultrasonic field near a wall," *IEEE transactions on ultrasonics, ferroelectrics, and frequency control*, vol. 51, no. 8, pp. 973–979, 2004.

[73] J. T. Belcik, B. H. Mott, A. Xie, Y. Zhao, S. Kim, N. J. Lindner, A. Ammi, J. M. Linden, and J. R. Lindner, "Augmentation of limb perfusion and reversal of tissue ischemia produced by ultrasound-mediated microbubble cavitation," *Circulation: Cardiovascular Imaging*, vol. 8, no. 4, p. e002979, 2015.

[74] D. E. Goertz, R. Karshafian, and K. Hynynen, "Antivascular effects of pulsed low intensity ultrasound and microbubbles in mouse tumors," in *2008 IEEE Ultrasonics Symposium*, pp. 670–673, IEEE, 2008.

[75] C. P. Keravnou, I. De Cock, I. Lentacker, M.-L. Izamis, and M. A. Averkiou, "Microvascular injury and perfusion changes induced by ultrasound and microbubbles in a machine-perfused pig liver," *Ultrasound in medicine & biology*, vol. 42, no. 11, pp. 2676–2686, 2016.

[76] D. E. Goertz, "An overview of the influence of therapeutic ultrasound exposures on the vasculature: high intensity ultrasound and microbubble-mediated bioeffects," *International Journal of Hyperthermia*, vol. 31, no. 2, pp. 134–144, 2015.

[77] F. Yuan, M. Leunig, S. K. Huang, D. A. Berk, D. Papahadjopoulos, and R. K. Jain, "Mirovascular permeability and interstitial penetration of sterically stabilized (stealth) liposomes in a human tumor xenograft," *Cancer research*, vol. 54, no. 13, pp. 3352–3356, 1994.